

Mathematical Modelling of Mechanotransduction via RhoA Signalling Pathway

Sofie Verhees¹, Chandrasekhar Venkataraman², Mariya Ptashnyk¹

¹Department of Mathematics, Heriot-Watt University, The Maxwell Institute for Mathematical Sciences, Edinburgh, UK; ²Department of Mathematics, University of Sussex, Brighton, UK

Abstract

We derive and simulate a mathematical model for mechanotransduction related to the Rho GTPase signalling pathway. The model addresses the bidirectional coupling between signalling processes and cell mechanics. A numerical method based on bulk-surface finite elements is proposed for the approximation of the coupled system of nonlinear reaction-diffusion equations, defined inside the cell and on the cell membrane, and the equations of elasticity. Our simulation results illustrate novel emergent features such as the strong dependence of the dynamics on cell shape, a threshold-like response to changes in substrate stiffness, and the fact that coupling mechanics and signalling can lead to the robustness of cell deformation to larger changes in substrate stiffness, ensuring mechanical homeostasis in agreement with experiments.

Introduction

Intercellular signalling processes constitute the mechanisms through which cells communicate with and respond to their environment. Hence, signalling pathways are important in all physiological activities of the cell, such as cell division, cell movement, the immune response, and tissue development [1]. Aberrant cell signalling can often result in the development of diseases [2]. It is therefore important to understand signalling phenomena. Recent studies have found that alongside biochemical reactions, mechanics plays an important role in many signalling pathways [3, 4]. This phenomena is referred to as mechanotransduction which, broadly speaking, is any process by which cells convert mechanical stimuli into chemical signals [5, 6].

A large number of recent works study the role of Rho GTPases, primarily RhoA, in mechanotransduction in relation to different mechanical cues: extracellular matrix (ECM) stiffness and viscoelasticity, tensile stress (stretching), compressive stress (compression), and shear stress (fluid flow shear), see e.g. [7, 8] for a review. Moreover, the coupling between biochemistry and mechanics is bidirectional, i.e., chemical signals can also affect the mechanical properties of the cell, such as molecules like focal adhesion kinases (FAKs) that influence F-actin dynamics and therefore the stiffness of the cell [9, 6, 10, 11].

The formidable complexity of the phenomena involved in mechanotransduction means that much about how the mechanics and the chemical processes of the cell communicate is not yet understood and mathematical modelling is crucial in this regard. Whilst the mathematical modelling of biochemical cell signalling processes is fairly well developed, e.g., [12, 13, 14], the study of mechanotransduction is comparatively more recent, see [15] for a review. Typically the modelling involves solving coupled systems of partial differential equations (PDEs) with reaction-diffusion equations modelling the biochemistry coupled to equations based on (visco)elastic constitutive laws for the mechanics. The progress of such efforts has been rapid, ranging from early models employing simplifications such as one-dimensional geometries [16, 17] to full three-dimensional simulations [18] using advanced computational techniques. Alongside continuum models, a number of recent works have employed discrete approaches such as spring-based models [19], or models that employ a Potts formalism [20, 21, 22]. Despite this rapid progress, the existing models typically make major simplifying assumptions such as assuming a constant stiffness of the ECM [18, 23, 24], as well as neglecting the two-way coupling in which signalling pathways affect the mechanics alongside mechanical cues inducing signalling processes.

In the present work, we seek to develop, analyse and simulate a model for mechanotransduction through the Rho GTPase signalling pathway which allows for a two-way coupling between the mechanics and the biochemistry. The dynamics of the signalling molecules FAK and RhoA are modelled using reaction-diffusion equations, where the ECM stiffness and elastic stresses of the cell activate FAK. Under simplifying assumptions, i.e., assuming no dependence on the cell elastic stresses, the biochemical component of the model is derived as a reduction of the model proposed in [18]. For the cell's mechanical properties, we assume an elastic constitutive relationship [25] and

allow the material properties to depend on the concentrations of the signalling molecules. We propose a numerical method based on bulk and surface finite elements [26] for the approximation of the model equations.

The results presented here show that our model can reproduce the qualitative results of [18], i.e., the mass of activated FAK and RhoA depend on ECM stiffness, with the dependence captured well by a Hill function. On the inclusion of the two-way coupling between signalling processes and cell mechanics, we observe novel dynamics, such as the conservation of cell deformation under different values of the ECM stiffness, which underlines the importance of including these more complex models of the mechanics. The role of mechanotransduction in homeostasis in biological processes has been discussed in a number of biological works, e.g., [5, 4, 27, 9, 10] and our work presents a concrete example of how modelling can help elucidate potential mechanisms that underlay the mechanical homeostasis. Homeostasis of cell deformation, as observed in simulations of our model, has been observed experimentally [28]. Our focus is on elastic constitutive assumptions for the mechanics of the cell to enhance clarity of exposition and to avoid unnecessary technical complexities. This can be extended to allow for other constitutive laws such as viscoelasticity of the cell and/or of the ECM as has been done elsewhere in the literature in simpler settings in 1D [16, 29]. This work thus serves as a starting point in modelling and analysis of the two-way coupling between mechanics and chemistry.

The paper is organised as follows. We first derive the reduced model for the Rho GTPase signalling pathway, based on the model proposed in [18]. Next, the mathematical model for the mechanotransduction related to the Rho GTPase signalling pathway is derived. Simulations of the model are presented in the section after. We conclude the paper with a discussion of the results. Details on the numerical method applied to simulate the model equations are given in [S1 Appendix](#), Section A.3.

Methods

A Mathematical model for the Rho GTPase signalling pathway

One of the main signaling pathways involved in mechanostraduction is the Rho GTPase pathway, responsible for many important cellular processes, e.g. motility, cell adhesion, polarisation, differentiation, remodelling of the exoskeleton, and the ECM [8]. The RhoA signalling pathway is activated through the activation of FAK in response to tension on integrins, which depends on ECM stiffness [1, 11].

Our model for mechanotransduction related to the RhoA-mediated intercellular signalling pathway is based on models developed in [18] and [24, 23]. To incorporate the interactions between mechanics and signalling processes, we extend the model proposed in [18] by considering elastic deformations of the cell. Activated FAK is downstream in the RhoA GTPase signalling pathway and hence the activation of RhoA is a function of activated FAK. The activation of RhoA results in ECM remodelling and deposition of new fibres, increasing ECM stiffness and hence activation of FAK [30]. FAK is expressed in the cytoplasm of the cell and is activated on the cell membrane. To simplify the model and focus only on the most significant aspects from the perspective of qualitative behaviour, we reduce the model for the RhoA signalling pathway of [18] that includes the dynamics of FAK, RhoA, ROCK, Myo, LIMK, mDia, Cofilin, F-actin and YAP/TAZ by considering only the dynamics of FAK and activated RhoA. Such a reduction is possible since other molecules considered in the full model of [18] do not influence the dynamics of FAK and RhoA. Our rationale behind considering a simplified model is to more clearly elucidate the emergent features that arise when mechanics is coupled with signalling. It is not challenging to incorporate other biochemical species or different reaction kinetics within the framework we propose.

We let $Y \subset \mathbb{R}^3$ denote the cytoplasm and $\Gamma = \partial Y$ the cell membrane. We denote by ϕ_d and ϕ_a the concentrations of inactive and active FAK, and by ρ_a the concentration of active RhoA. We recall that FAK, both active and inactive, is assumed to be cytoplasm resident and activated RhoA membrane resident. Our reduced model for the biochemistry consists of the following system of reaction-diffusion equations

$$\begin{aligned}
\partial_t \phi_d - D_1 \Delta \phi_d &= k_1 \phi_a && \text{in } Y, t > 0, \\
\partial_t \phi_a - D_2 \Delta \phi_a &= -k_1 \phi_a && \text{in } Y, t > 0, \\
D_1 \nabla \phi_d \cdot \nu &= -n_r k_2 \phi_d - n_r k_3 \frac{E}{C + E} \phi_d && \text{on } \Gamma, t > 0, \\
D_2 \nabla \phi_a \cdot \nu &= n_r k_2 \phi_d + n_r k_3 \frac{E}{C + E} \phi_d && \text{on } \Gamma, t > 0, \\
\partial_t \rho_a - D_3 \Delta_\Gamma \rho_a &= -k_4 \rho_a + n_r k_5 ((\gamma \phi_a)^n + 1) \left(\frac{M_\rho}{|Y|} - \frac{\rho_a}{n_r} \right) && \text{on } \Gamma, t > 0, \\
\phi_d(0, x) &= \phi_d^0(x), \quad \phi_a(0, x) = \phi_a^0(x) \quad \text{in } Y, \quad \rho_a(0, x) = \rho_a^0(x) \quad \text{on } \Gamma,
\end{aligned} \tag{1}$$

where Δ_Γ is the Laplace Beltrami operator modelling diffusion on the surface Γ , see e.g. [26], $n_r = |Y|/|\Gamma|$ is the ratio between the volume of the cytoplasm and the area of the cell membrane, k_1, k_4 are deactivation and k_2, k_3, k_5 are activation constants, E is the substrate stiffness, D_1, D_2, D_3 are the diffusion constants, C, n and γ are positive constants, $\phi_d^0(x), \phi_a^0(x)$ and $\rho_a^0(x)$ are bounded nonnegative functions, and $\frac{M_\rho}{|Y|} - \frac{\rho_a}{n_r}$ is an approximation for deactivated RhoA (ρ_d) on the surface with $M_\rho = \int_Y \rho_d^0 \, dx + \int_\Gamma \rho_d^0 \, ds$ the total mass of RhoA, a quantity conserved in the full model of [18] and assumed to be conserved here. Simulations illustrating the agreement between results obtained using the reduced model (1) with those of [18] for the full model are presented in [S1 Appendix](#), Section A.1.

Mathematical model for mechanotransduction

As a starting point for the mechanics, we consider small deformations and hence, assume a linear elastic constitutive law for the mechanics of the cell. Although viscoelastic or poroelastic behaviour of cells is proposed in many works [31, 32], linear elasticity is often chosen for modelling simplicity and it can yield results consistent with experimental observations [33, 34, 35]. Our focus is modelling a bidirectional coupling between cell stiffness and signalling processes, a minimal model assuming a linear elastic law for the cell mechanics is therefore sufficient for this work, as it avoids unnecessary complications that arise from the consideration of viscous stresses. To demonstrate that our results remain relevant under more complex assumptions, a linear viscoelastic model is presented and simulated in Section A.7 in [S1 Appendix](#). We note that for the corresponding simulation results, the qualitative behaviour in both cases, linear elastic and linear viscoelastic, is the same.

An important simplification that arises under the small deformations assumption inherent in this work is that the dynamics of the signalling molecules may be effectively considered on the reference configuration with no additional terms arising due to the deformation. Models where the assumption of small deformations is relaxed will be addressed in future studies.

The cell nucleus plays an important role in governing the mechanical properties of the cell [36, 37], whilst we predominantly neglect this in the present work, in [S1 Appendix](#), Section A.5, we have included simulations of the model with a ‘passive’ nucleus that is considered to be more rigid than the cytoplasm.

It has been shown that the stiffness of the cell increases as F-actin increases [18]. F-actin is downstream from activated FAK and, as apparent from the results in [18], we can use activated FAK as a proxy for F-actin. Therefore, we assume that the Young’s modulus E_c of the cell is a function of the activated FAK concentration. Based on experimental observations [38] and numerical simulations [18], we propose

$$E_c = E_c(\phi_a) = k_7(1 + (k_8\phi_a)^p), \quad (2)$$

where k_7, k_8 and p are non-negative constants. Then for elastic deformations of the cell, we have

$$-\nabla \cdot \sigma(u) = 0 \quad \text{in } Y, \quad (3)$$

with

$$\sigma(u) = \lambda(\phi_a)(\nabla \cdot u)I + 2\mu(\phi_a)(\nabla u + (\nabla u)^T)$$

and the Lame constants λ and μ are given by

$$\lambda(\phi_a) = \frac{E_c(\phi_a)\nu_c}{(1 + \nu_c)(1 - 2\nu_c)}, \quad \mu(\phi_a) = \frac{E_c(\phi_a)}{2(1 + \nu_c)},$$

where ν_c is the Poisson ratio of the cell.

Activated RhoA regulates remodelling of stress fibres inside the cell and stabilisation of actin filaments [39, 40, 41, 43]. This mechanism is modelled by the stress on the boundary being dependent on activated RhoA concentration

$$\sigma(u)\nu = k_6 \mathbb{P}(\rho_a \nu) \quad \text{on } \Gamma, \quad (4)$$

where k_6 is a positive constant, \mathbb{P} is a projection on the space orthogonal to the space of rigid deformations, i.e. rotations and translations. Alongside models where the cell is allowed to deform freely, to model a typical experimental set-up where cells are placed on a rigid substrate, we consider

$$u \cdot \nu = 0, \quad \Pi_\tau(\sigma(u)\nu) = 0 \quad \text{on } \Gamma_0, \quad (5)$$

together with condition Eq (4) on $\Gamma \setminus \Gamma_0$, where $\Pi_\tau(w) = w - (w \cdot \nu)\nu$ denotes the tangential projection of vector w . In this work, we choose $\Gamma_0 = \Gamma \cap \{x \in \mathbb{R}^3 | x_3 = 0\}$ to simulate a rigid substrate.

It has been shown that an increased contractility is associated with increased activated FAK, see e.g. [39]. Thus we assume that FAK is activated by the stress of the cell and as a proxy for the cytosolic stress we use the positive part of trace of the Cauchy stress tensor $\text{tr}(\sigma)_+$, where $\text{tr}(\sigma)$ is the first stress invariant and the positive part reflects the fact that extension rather than compression causes the activation of FAK. This modifies the system in Eq (1) to

$$\begin{aligned}
\partial_t \phi_d - D_1 \Delta \phi_d &= k_1 \phi_a - C_1 \text{tr}(\sigma)_+ \phi_d && \text{in } Y, t > 0, \\
\partial_t \phi_a - D_2 \Delta \phi_a &= -k_1 \phi_a + C_1 \text{tr}(\sigma)_+ \phi_d && \text{in } Y, t > 0, \\
D_1 \nabla \phi_d \cdot \nu &= -n_r k_2 \phi_d - n_r k_3 \frac{E}{C + E} \phi_d && \text{on } \Gamma, t > 0, \\
D_2 \nabla \phi_a \cdot \nu &= n_r k_2 \phi_d + n_r k_3 \frac{E}{C + E} \phi_d && \text{on } \Gamma, t > 0, \\
\partial_t \rho_a - D_3 \Delta_\Gamma \rho_a &= -k_4 \rho_a + n_r k_5 ((\gamma \phi_a)^n + 1) \left(\frac{M_\rho}{|Y|} - \frac{\rho_a}{n_r} \right) && \text{on } \Gamma, t > 0, \\
\phi_d(0, x) &= \phi_d^0(x), \quad \phi_a(0, x) = \phi_a^0(x) \quad \text{in } Y, \quad \rho_a(0, x) = \rho_a^0(x) \quad \text{on } \Gamma,
\end{aligned} \tag{6}$$

where $v_+ = \max\{v, 0\}$. We can prove existence, uniqueness and boundedness of solutions to the system in Eqs (3)-(6) which we intend to report on elsewhere.

Initial and boundary conditions and parametrization

Using the model in Eqs (3)-(6) we investigate different scenarios demonstrating the interactions between mechanics and signalling processes. First, we consider the impact of the cell Young's modulus E_c and compare the dynamics when considering a constant E_c versus the case where E_c depends on activated FAK as defined in Eq (2). We also model the effect of the stress on the signalling molecules FAK and simulate equations Eq (6) for $C_1 = 0$ (kPa s) $^{-1}$ and $C_1 = 0.1$ (kPa s) $^{-1}$, respectively. Additionally we consider two experimental scenarios: (i) the cell is placed on a rigid substrate, modelled by the boundary conditions Eq (4) on $\Gamma \setminus \Gamma_0$ and Eq (5) on Γ_0 or (ii) the cell is embedded in an agar substrate and we apply the force boundary condition Eq (4) on the entire cell membrane. We also distinguish between two different stimuli, similar to [18], (i) the so called '2xD stimulus', where the substrate stiffness is only applied to the bottom of the cell, i.e. E is nonzero only on Γ_0 , and (ii) the '3D stimulus' where the cell is embedded in an agar (substrate) and the impact of the substrate stiffness on the signalling processes is considered on the whole cell membrane. To analyse the impact of the cell shape on the dynamics of signalling molecules and mechanical deformations we consider both axisymmetric cells and polarised cells with a lamellipodium like shape. The diameter of the cell is larger for the lamellipodium cells such that the volume is similar to the axisymmetric cells.

The parameters are chosen as in Table 1. For numerical simulations, we use a Finite Element Method to discretize in space and a semi-implicit Euler method to discretize in time, with the mesh size $h = 2.94 \mu\text{m}$ and time step $\Delta t = 0.5 \text{ s}$. Details on the numerical scheme and benchmark computations demonstrating the accuracy of the approach for a problem with a known solution are given in [S1 Appendix](#), Section A.3.

Table 1: Parameter values for simulations of the model in Eqs (3)-(6).

(a) Parameters inherited from the model in Eq (1) that are identical to [18]. Because the goal is to compare and extend upon the model of [18], we choose the values to be the same as [18], which are based on literature and fitting to data. The exception are D_1 and D_2 , which is discussed in [S1 Appendix](#), Section A.1.

Parameters	Value
ϕ_d^0	$0.7 \mu\text{mol}/\text{dm}^3$
ϕ_a^0	$0.3 \mu\text{mol}/\text{dm}^3$
ρ_a^0	$6 \cdot 10^{-7} \mu\text{mol}/\text{dm}^2$
ρ_d^0	$1 \mu\text{mol}/\text{dm}^3$
D_1	$4 \mu\text{m}^2/\text{s}$
D_2	$4 \mu\text{m}^2/\text{s}$
D_3	$0.3 \mu\text{m}^2/\text{s}$
k_1	0.035 s^{-1}
k_2	0.015 s^{-1}
k_3	0.379 s^{-1}
k_4	0.625 s^{-1}
k_5	0.0168 s^{-1}
E	$0.1, 5.7, 7 \cdot 10^6 \text{ kPa}$
C	3.25 kPa
n	5
γ	$8.8068 \text{ dm}^3/\mu\text{mol}$
axisymmetric shape	$ Y $
	$1193 \mu\text{m}^3$
	$ \Gamma $
	$1020 \mu\text{m}^2$
lamellipodium shape	$ Y $
	$1099 \mu\text{m}^3$
	$ \Gamma $
	$1115 \mu\text{m}^2$

(b) Parameter values for parameters introduced in this paper. A brief robustness analysis is performed on all parameters introduced in the coupled model in Eqs (3)-(6), see [S1 Appendix](#), Section A.6.

Parameters	Value	Reference/ Justification
C_1	$0.1 (\text{kPa s})^{-1}$	range $0 - 2 (\text{kPa s})^{-1}$ is explored in results
k_6	0.1 s^{-1}	fitted to yield magnitude of deformation range $0 - 10 \mu\text{m}$ [18]
k_7	0.2 kPa	fitted to results for ϕ_a in [18]
k_8	$2.4245 \text{ dm}^3/\mu\text{mol}$	fitted to results for ϕ_a in [18]
p	2.6	fitted to results for ϕ_a and F-actin in [18] and [38]
ν_c	0.3	estimated $0.17 - 0.66$ [42]

Results

Numerical simulations with 2xD stimulus

First we look at the results that would most reflect a cell on a substrate in vitro. Here, the substrate stiffness appears as a stimulus only on the bottom boundary of the cell, i.e. E is nonzero only on Γ_0 , and deformation is restricted in the vertical direction at the bottom boundary of the cell. The results for the axisymmetric shape of the cell are found in Fig 1, whereas results for the lamellipodium shape are presented in Fig 2. Note that results for ϕ_a and ρ_a when $E_c = 0.6 \text{ kPa}$ and $C_1 = 0 (\text{kPa s})^{-1}$ are identical to the one without mechanics in [S1 Appendix](#), Section A.1. In this case, we see that the magnitude of the deformation $|u|$ is largest at the edge of the cell. The cell expands axisymmetrically at the base. As expected, the expansion is larger for higher concentrations of ϕ_a . For a lower substrate stiffness, $E = 0.1 \text{ kPa}$, the cell barely expands. When $C_1 = 0.1 (\text{kPa s})^{-1}$, the concentrations of ϕ_a and ρ_a and the magnitude of the deformation $|u|$ increase, with a bigger increase for lower substrate stiffness and a smaller increase for larger substrate stiffness. When comparing $E_c = 0.6 \text{ kPa}$ and $E_c = f(\phi_a)$, the deformations show similar patterns, expanding at the base of the cell, however, the magnitude of the deformation is much lower in the case $E_c = f(\phi_a)$. This is probably because $E_c = f(\phi_a) \approx 0.6 \text{ kPa}$ for a small substrate stiffness E , but is doubled in magnitude for larger substrate stiffness, see Fig 3. The larger cell Young's modulus E_c means it is harder for the cell to deform, resulting in a lower magnitude of deformation. This difference illustrates that, unlike the constant Young's modulus case, a concentration-dependent Young's modulus allows for potential homeostasis and adaptation of cell mechanics to different values of the substrate stiffness [28].

For the two-way couplings between the mechanics and chemistry, i.e. $E_c = f(\phi_a)$ and $C_1 = 0.1 (\text{kPa s})^{-1}$, we see similar results for the deformation as when $E_c = f(\phi_a)$ and $C_1 = 0 (\text{kPa s})^{-1}$. The main difference is that the deformation for $E = 0.1 \text{ kPa}$ is now at a similar magnitude as for the larger substrate stiffnesses, demonstrating the importance of the signalling processes in the adaptation of cell mechanics to changing environmental conditions.

Comparing the simulation results for the two different shapes in Fig 1 and 2, the concentration of activated RhoA, ρ_a , is slightly lower for the lamellipodium shape. For the lamellipodium shape, we observe the largest deformations at the corners furthest from the nucleus.

Fig 3 summarises the results at time $T = 100$ s by plotting the mean, $\frac{1}{|\Omega|} \int_{\Omega} \cdot dx$, of $E_c = f(\phi_a)$, the volume change $\text{div}(u)$, ϕ_a , and ρ_a as functions of the substrate stiffness E , with the bars being the range of these variables, for different values of the constant C_1 in the activation of FAK by the cell stress. As expected, an increase in C_1 results in an increase in the concentration of activated FAK, ϕ_a . The dependence of ϕ_a on the substrate stiffness E , especially for $C_1 = 0$ (kPa s) $^{-1}$ and $C_1 = 0.5$ (kPa s) $^{-1}$, resembles a Hill function representing a threshold response. This agrees with simulations in [18] which themselves fit experimental observations presented in [44]. For most of the cases, the results for the lamellipodium shape are very similar to the results for the axisymmetric shape. However, for $C_1 = 0.1$ (kPa s) $^{-1}$, the magnitude of the threshold-like response in all variables is bigger in the lamellipodium case. In terms of the Young's modulus, when $E_c = 0.6$ kPa we observe much larger volume changes than when $E_c = f(\phi_a)$ in all the numerical experiments.

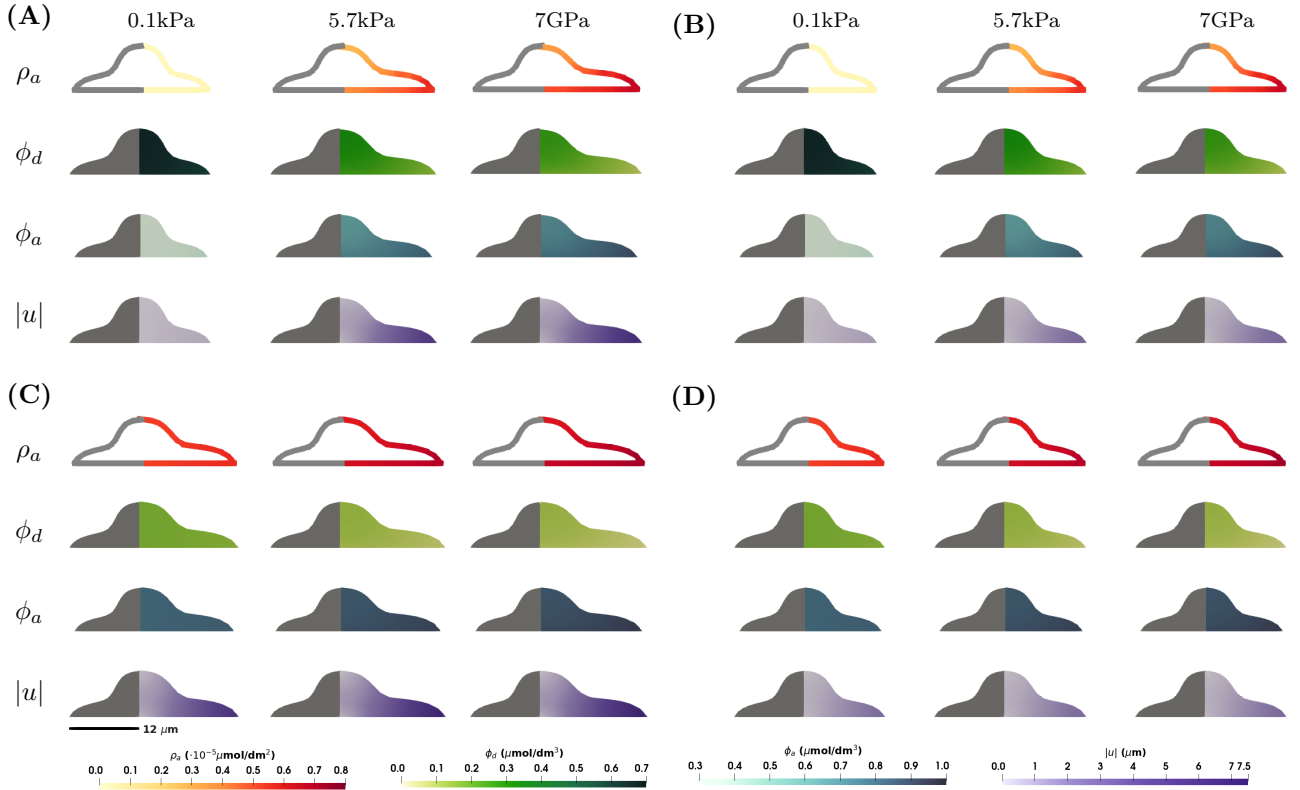


Figure 1: Numerical simulation results showing ρ_a , ϕ_d , ϕ_a and $|u|$ for the model in Eqs (3)-(6) for the axisymmetric shape and in the case of 2xD stimulus at a steady state at $T = 100$ s. Four different scenarios are considered: (A) $C_1 = 0$ (kPa s) $^{-1}$ ($\sigma \not\rightarrow \phi_a$) and $E_c = 0.6$ kPa ($\phi_a \not\rightarrow E_c$); (B) $C_1 = 0$ (kPa s) $^{-1}$ ($\sigma \not\rightarrow \phi_a$) and $E_c = f(\phi_a)$ ($\phi_a \rightarrow E_c$); (C) $C_1 = 0.1$ (kPa s) $^{-1}$ ($\sigma \rightarrow \phi_a$) and $E_c = 0.6$ kPa ($\phi_a \not\rightarrow E_c$); (D) $C_1 = 0.1$ (kPa s) $^{-1}$ ($\sigma \rightarrow \phi_a$) and $E_c = f(\phi_a)$ ($\phi_a \rightarrow E_c$). Within each subfigure, the rows represent ρ_a , ϕ_d , ϕ_a and $|u|$ on a cross-section of the plane $x_1 = 0$ of the axisymmetric cell, and the columns represent $E = 0.1, 5.7, 7 \cdot 10^6$ kPa. Parameter values as in Table 1.

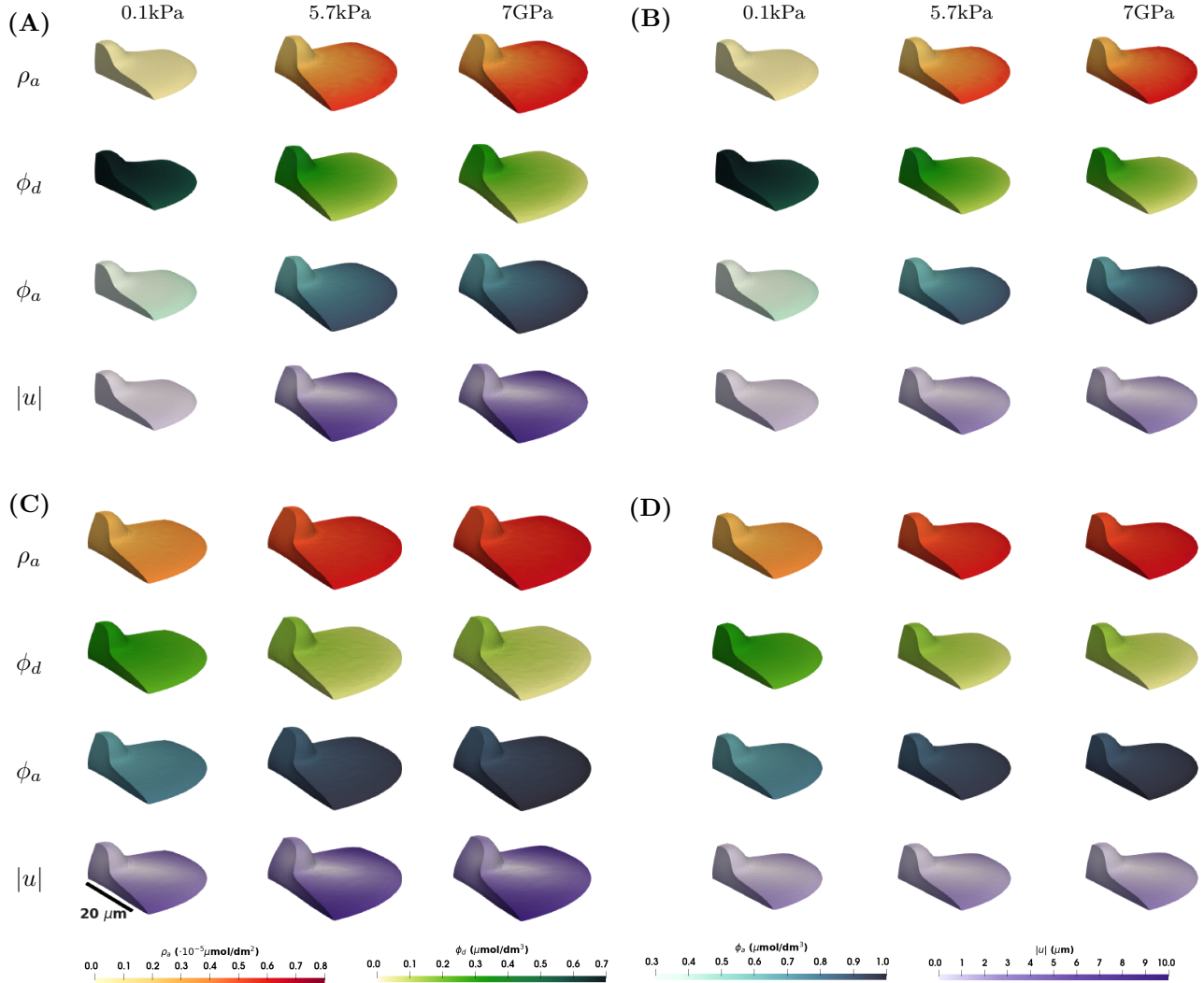


Figure 2: Numerical simulation results showing ρ_a , ϕ_d , ϕ_a and $|u|$ for the model in Eqs (3)-(6) for the lamellipodium shape and in the case of 2xD stimulus at a steady state at $T = 100$ s. Four different scenarios are considered: (A) $C_1 = 0$ $(\text{kPa s})^{-1}$ ($\sigma \not\rightarrow \phi_a$) and $E_c = 0.6$ kPa ($\phi_a \not\rightarrow E_c$); (B) $C_1 = 0$ $(\text{kPa s})^{-1}$ ($\sigma \not\rightarrow \phi_a$) and $E_c = f(\phi_a)$ ($\phi_a \rightarrow E_c$); (C) $C_1 = 0.1$ $(\text{kPa s})^{-1}$ ($\sigma \rightarrow \phi_a$) and $E_c = 0.6$ kPa ($\phi_a \not\rightarrow E_c$); (D) $C_1 = 0.1$ $(\text{kPa s})^{-1}$ ($\sigma \rightarrow \phi_a$) and $E_c = f(\phi_a)$ ($\phi_a \rightarrow E_c$). Within each subfigure, the rows represent ρ_a , ϕ_d , ϕ_a and $|u|$ on the surface of the cell, and the columns represent $E = 0.1, 5.7, 7 \cdot 10^6$ kPa. Parameter values as in Table 1.

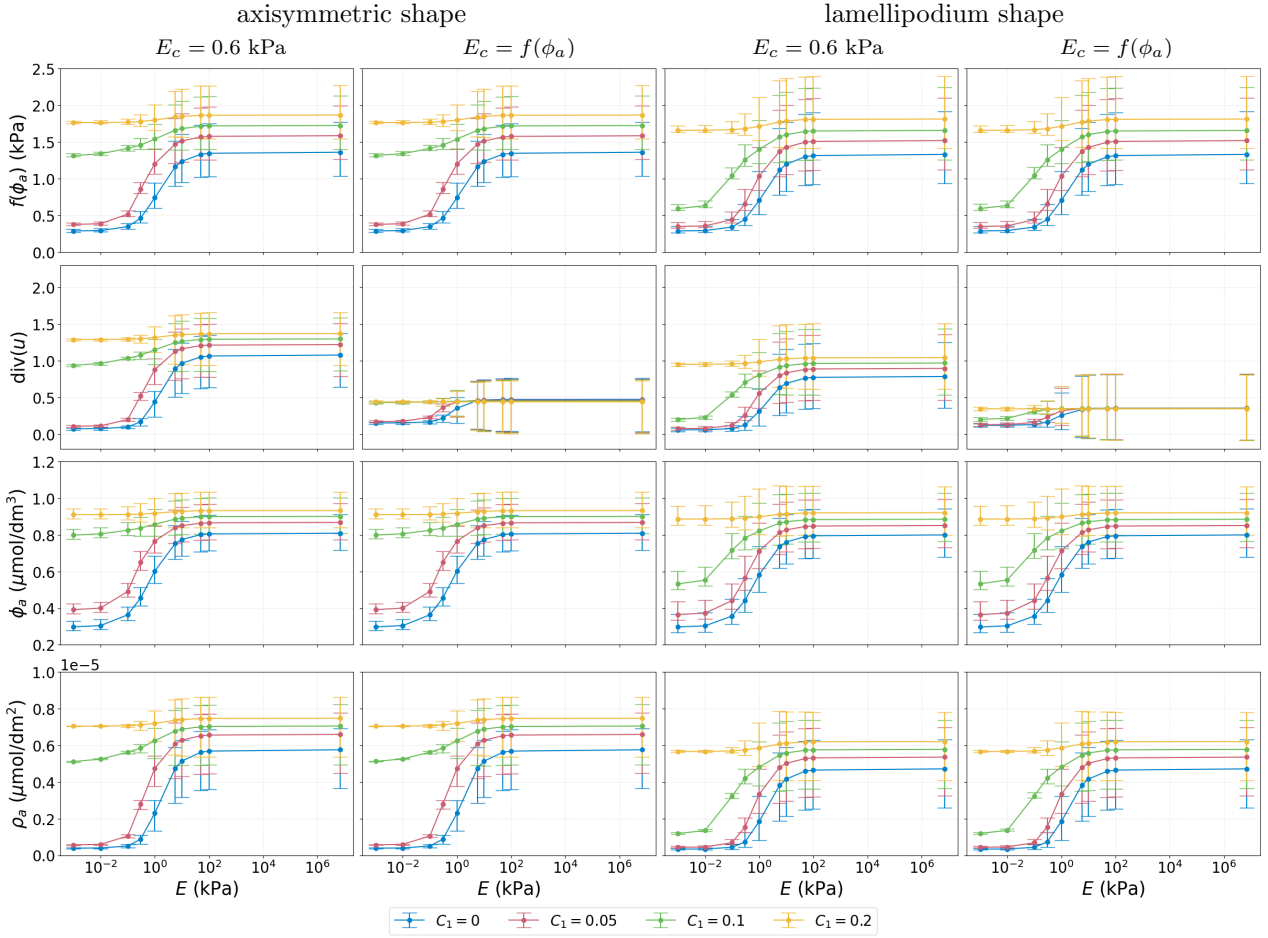


Figure 3: **Simulation results showing the mean, $\frac{1}{|\Omega|} \int_{\Omega} \cdot \, dx$, min and max values of $f(\phi_a)$, $\text{div}(u)$, ϕ_a and ρ_a as functions of substrate stiffness E .** We consider different couplings with four different values for C_1 and two different shapes at $T = 100$ s by which time the results are at a steady state. All other parameter values as in Table 1.

Numerical simulations for the 3D stimulus case on a rigid substrate

In numerical simulations for a 3D stimulus on a rigid substrate, the substrate stiffness affects the whole cell membrane and we consider the boundary conditions Eq (4) on $\Gamma \setminus \Gamma_0$ and Eq (5) on Γ_0 . The results for numerical experiments can be found in Fig 4-5. Overall, the concentrations ϕ_a and ρ_a are larger than in the case of the 2xD stimulus, which is in line with the results in [18]. The higher concentrations of ρ_a results in larger deformations, where the maximum magnitude of the deformation in the case of the 2xD stimulus was $7 \mu\text{m}$, see Fig 1, while the maximum magnitude of the deformation in the case of the 3D stimulus is $7.5 \mu\text{m}$, see Fig 4. Similar behaviour is observed for the lamellipodium shape, see Fig 2 and in S1 Fig. Another difference between two cases are larger variations in concentration and a larger difference between maximal and minimal values in the case of the 2xD stimulus than in the case of 3D stimulus, see Fig 3 and 5. Similar behaviour is observed also in the model for the signalling processes without mechanics, see S1 Appendix, Section A.1.

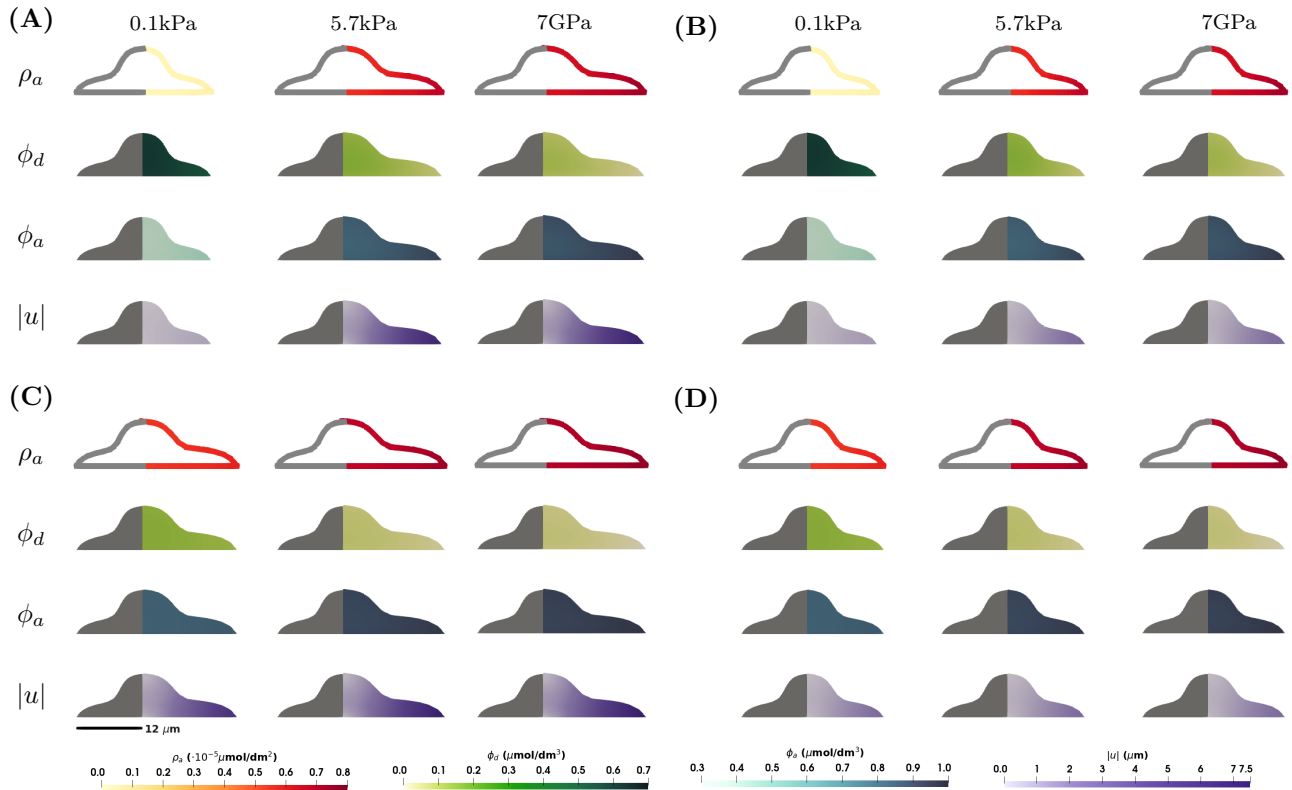


Figure 4: Numerical simulation results showing ρ_a , ϕ_d , ϕ_a and $|u|$ for the model in Eqs (3)-(6) for the axisymmetric shape and in the case of the 3D stimulus at a steady state at $T = 100 \text{ s}$. Four different scenarios are considered: (A) $C_1 = 0 \text{ (kPa s)}^{-1}$ ($\sigma \not\propto \phi_a$) and $E_c = 0.6 \text{ kPa}$ ($\phi_a \not\propto E_c$); (B) $C_1 = 0 \text{ (kPa s)}^{-1}$ ($\sigma \not\propto \phi_a$) and $E_c = f(\phi_a)$ ($\phi_a \rightarrow E_c$); (C) $C_1 = 0.1 \text{ (kPa s)}^{-1}$ ($\sigma \rightarrow \phi_a$) and $E_c = 0.6 \text{ kPa}$ ($\phi_a \not\propto E_c$); (D) $C_1 = 0.1 \text{ (kPa s)}^{-1}$ ($\sigma \rightarrow \phi_a$) and $E_c = f(\phi_a)$ ($\phi_a \rightarrow E_c$). Within each subfigure, the rows represent ρ_a , ϕ_d , ϕ_a and $|u|$ on a cross-section of the plane $x_1 = 0$ of the axisymmetric cell, and the columns represent $E = 0.1, 5.7, 7 \cdot 10^6 \text{ kPa}$. Parameter values as in Table 1.

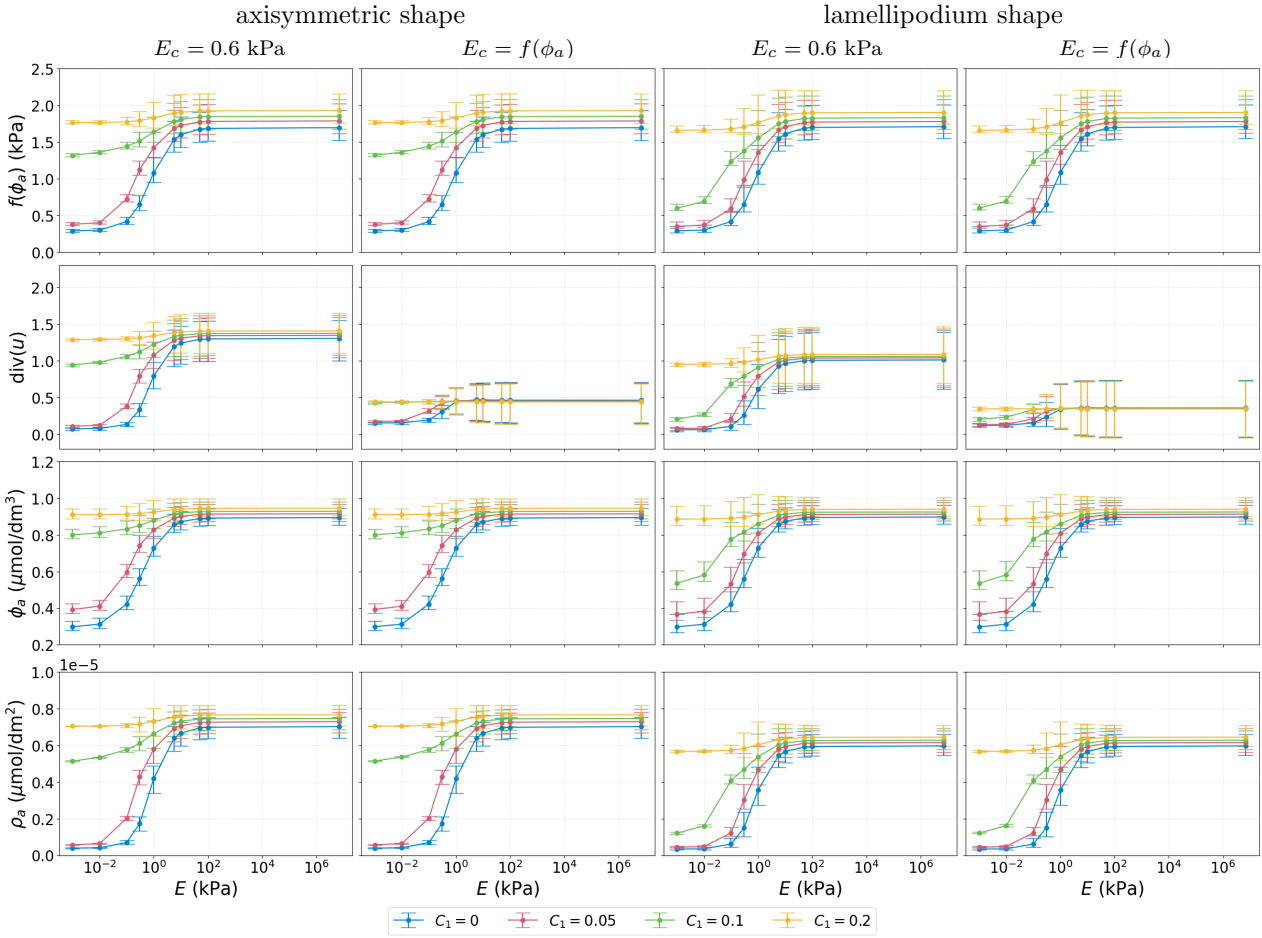


Figure 5: **Simulation results showing the mean, $\frac{1}{|\Omega|} \int_{\Omega} \cdot dx$, min and max values of $f(\phi_a)$, $\text{div}(u)$, ϕ_a and ρ_a as functions of substrate stiffness E .** We consider different couplings with four different values for C_1 and two different shapes at $T = 100$ s by which time the results are at a steady state. All other parameter values as in Table 1.

Numerical simulations for the model in Eqs(3), (4), and (6).

To investigate a setting more close to a cell in vivo, we consider the coupled model in Eqs (3)-(4), (6) with force boundary conditions on the whole cell membrane, without restricting the deformation on the bottom of the cell.

Numerical simulations in the case of 3D stimulus.

Simulation results for a 3D stimulus that models a cell surrounded by the extracellular matrix are presented in Fig 6-7. Corresponding results of the evolution of the mean of $f(\phi_a)$, $\text{div}(u)$, ϕ_a and ρ_a can be found in [S1 Appendix](#), Section A.2. The results show the same differences between the different couplings as in Fig 4-5. Comparing Fig 4 and 6, the results for the concentrations ϕ_a and ρ_a are indistinguishable, however there is a clear difference in deformation of the bottom of the cell and in the case of the fixed vertical deformations the magnitude of the deformation at the base of the cell is slightly lower than in the case of force boundary conditions. The same differences are observed for the lamellipodium shape case, see [S1 Fig](#) and [S2 Fig](#). The concentrations of the signalling molecules are also less sensitive to parameter changes than the volume change, as can be seen from the parameter analysis in [S1 Appendix](#), Section A.6. Comparing Fig 5 and 7, the main difference is in the behaviour of $\text{div}(u)$ as a function of E . Even though the average volume change is the same, we see differences in the maximum and minimum values of the local volume change across the domain. In particular, the maximum local volume change when considering the model with a partially fixed boundary is larger and is located on the base of the cell, while the maximum local volume change when considering the model with the force boundary conditions is smaller, but the cell deforms more evenly in all directions.

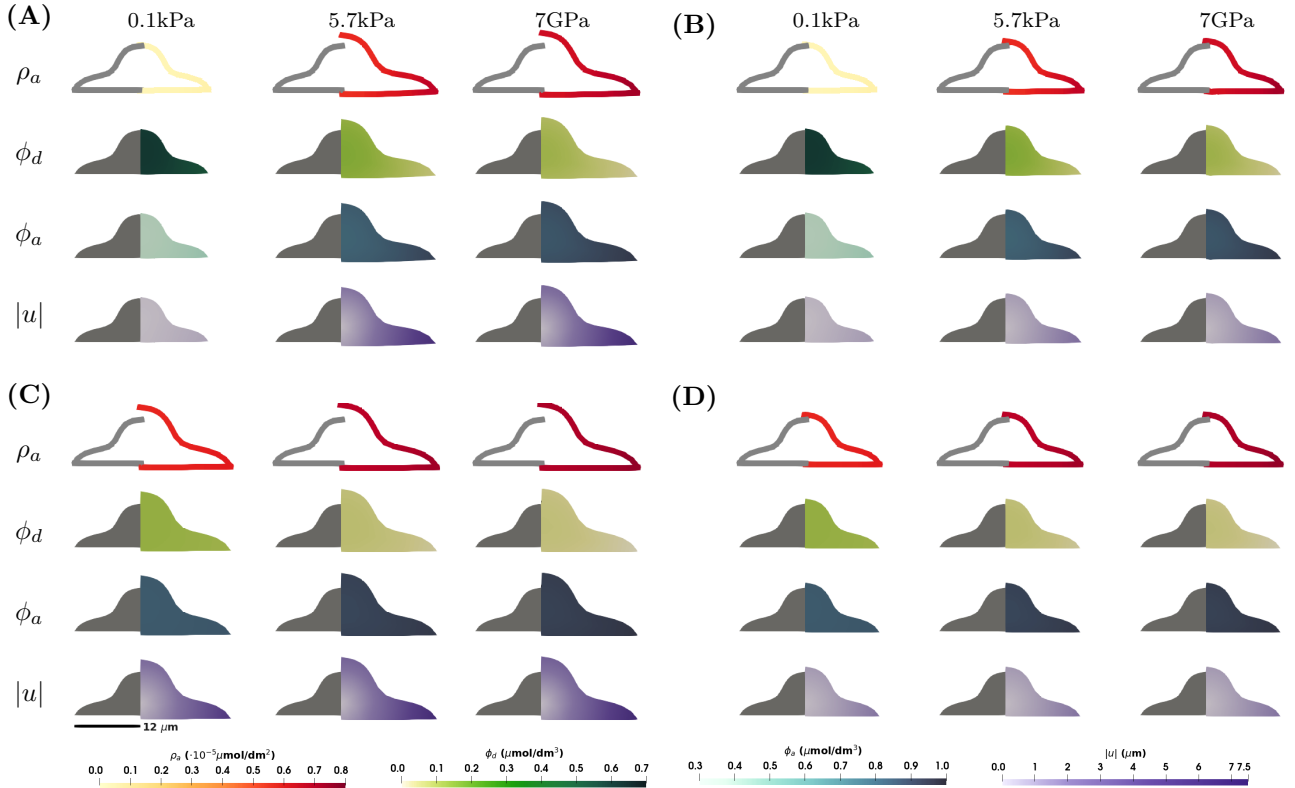


Figure 6: Numerical simulation results showing ρ_a , ϕ_d , ϕ_a and $|u|$ for the model in Eqs (3), (4), and (6) for the axisymmetric shape and in the case of the 3D stimulus at a steady state at $T = 100$ s. Four different scenarios are considered: **(A)** $C_1 = 0$ $(\text{kPa s})^{-1}$ ($\sigma \not\rightarrow \phi_a$) and $E_c = 0.6$ kPa ($\phi_a \not\rightarrow E_c$); **(B)** $C_1 = 0$ $(\text{kPa s})^{-1}$ ($\sigma \not\rightarrow \phi_a$) and $E_c = f(\phi_a)$ ($\phi_a \rightarrow E_c$); **(C)** $C_1 = 0.1$ $(\text{kPa s})^{-1}$ ($\sigma \rightarrow \phi_a$) and $E_c = 0.6$ kPa ($\phi_a \not\rightarrow E_c$); **(D)** $C_1 = 0.1$ $(\text{kPa s})^{-1}$ ($\sigma \rightarrow \phi_a$) and $E_c = f(\phi_a)$ ($\phi_a \rightarrow E_c$). Within each subfigure, the rows represent ρ_a , ϕ_d , ϕ_a and $|u|$ on a cross-section of the plane $x_1 = 0$ of the axisymmetric cell, and the columns represent $E = 0.1, 5.7, 7 \cdot 10^6$ kPa. Parameter values as in Table 1.

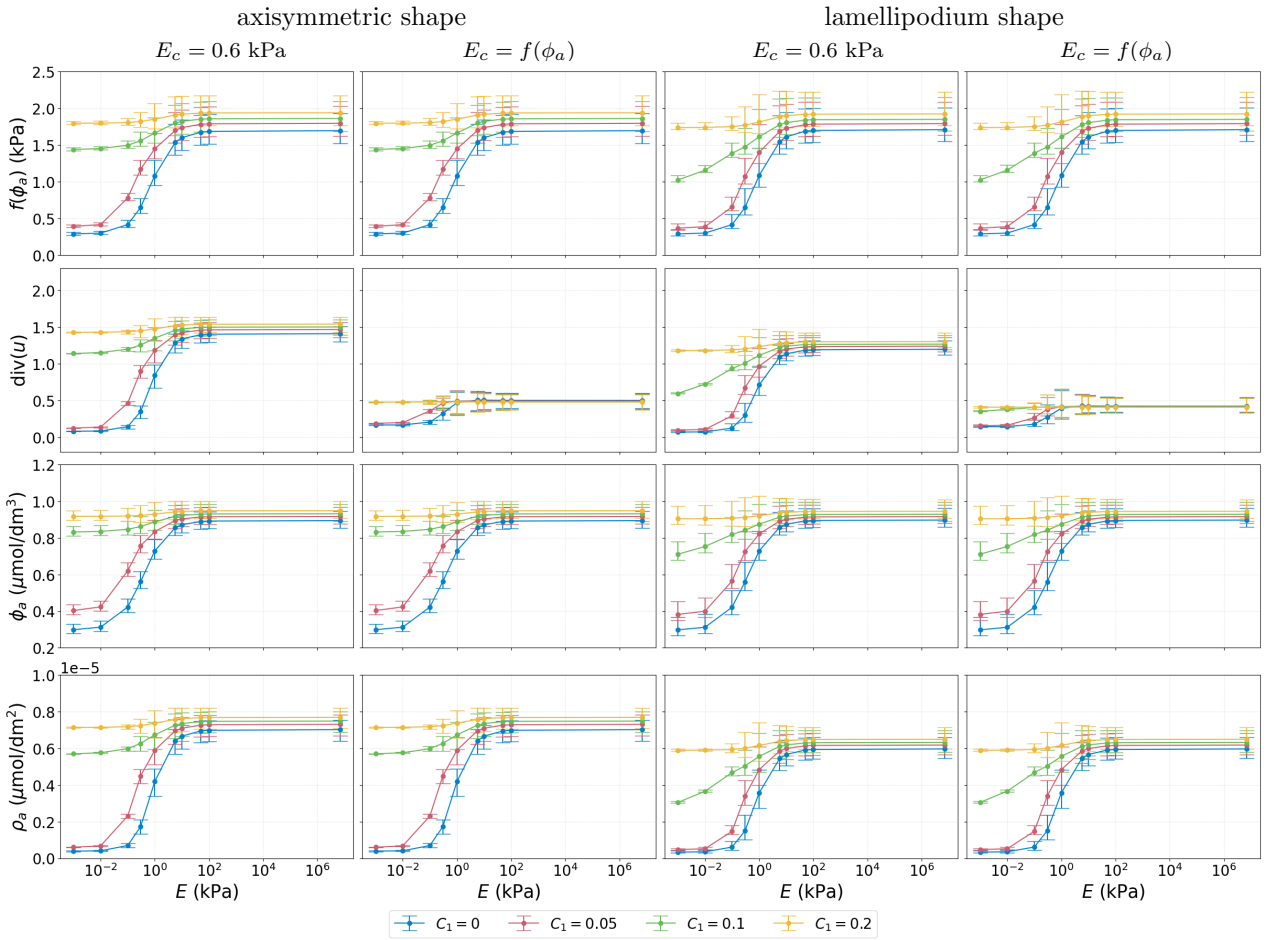


Figure 7: **Simulation results showing the mean, $\frac{1}{|\Omega|} \int_{\Omega} \cdot \, dx$, min and max values of $f(\phi_a)$, $\text{div}(u)$, ϕ_a and ρ_a as functions of substrate stiffness E , in the case of the model in Eqs (3), (4) and (6) and 3D stimulus.** We consider different couplings, four different values for C_1 , and two different shapes at $T = 100 \text{ s}$ by which time the results are at a steady state. All other parameter values as in Table 1.

Numerical simulations in the case of 2xD stimulus

In Fig 8, and in S3 Fig and S4 Fig we report on simulation results in the case of 2xD stimulus and force boundary conditions applied to the entire boundary. For the concentrations, the results are similar to the results in the case of 2xD stimulus and no vertical deformation on the bottom of the cell, see Fig 1 and 8. However, the results for the deformation are different compared to the previous results. In Fig 8, the cell does not just expand but changes shape as the edges of the cell deform upwards, which is not possible in the case of the partially fixed boundary as we assume no vertical deformation at the base. The deformation of the cell upwards can also be observed in the case of the 3D stimulus, but it is smaller due to the impact of the ECM surrounding the cell, see Fig 6. We observe that for $C_1 = 0$ $(\text{kPa s})^{-1}$ the cell deforms upwards a little more than for $C_1 = 0.1$ $(\text{kPa s})^{-1}$. This is due to the larger variation in the concentration ρ_a for $C_1 = 0$ $(\text{kPa s})^{-1}$ compared to $C_1 = 0.1$ $(\text{kPa s})^{-1}$. The same features are observed for the lamellipodium shape, see Fig 2, and in S2 Fig, S3 Fig and S4 Fig.

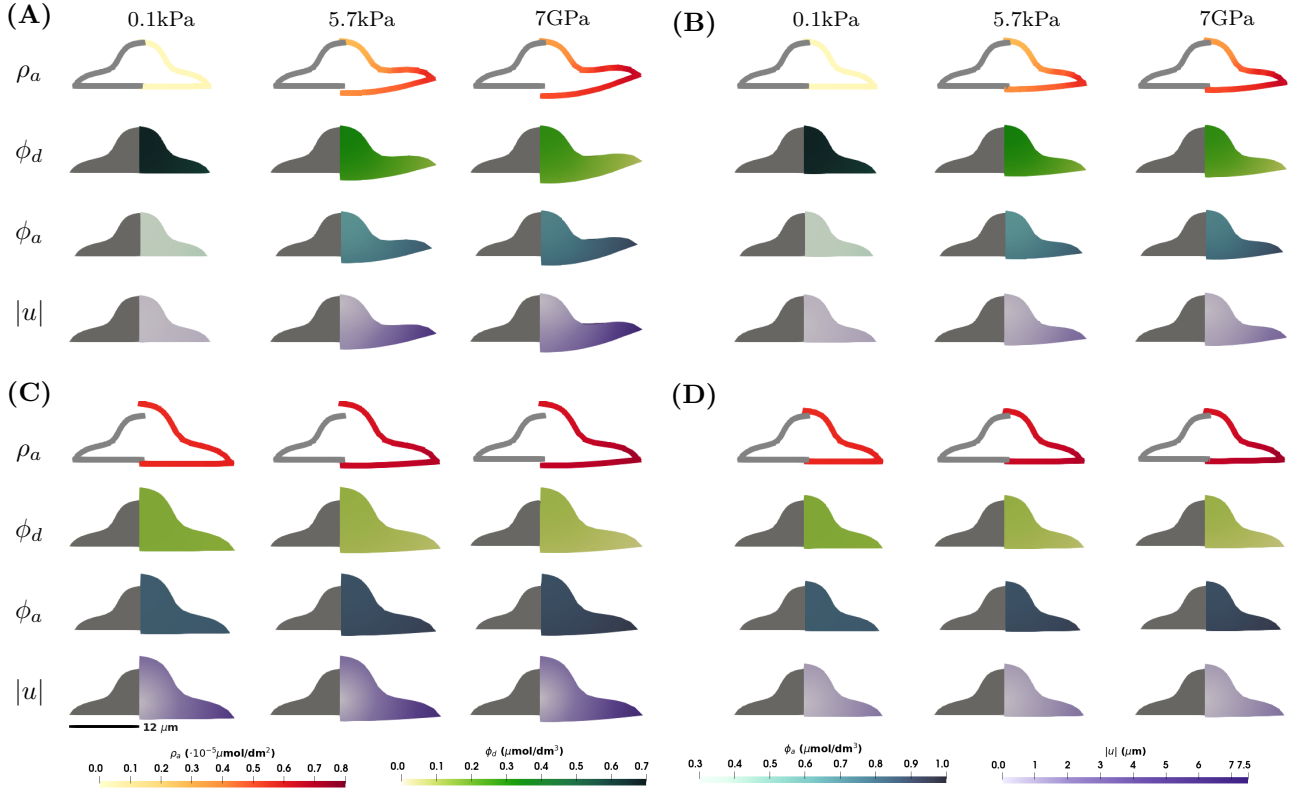


Figure 8: Numerical simulation results showing ρ_a , ϕ_d , ϕ_a and $|u|$ simulation results showing ϕ_a and ρ_a for the model in Eqs (3), (4), and (6) for the axisymmetric shape and in the case of 2xD stimulus at a steady state at $T = 100$ s. Four different scenarios are considered: (A) $C_1 = 0$ $(\text{kPa s})^{-1}$ ($\sigma \not\rightarrow \phi_a$) and $E_c = 0.6$ kPa ($\phi_a \not\rightarrow E_c$); (B) $C_1 = 0$ $(\text{kPa s})^{-1}$ ($\sigma \not\rightarrow \phi_a$) and $E_c = f(\phi_a)$ ($\phi_a \rightarrow E_c$); (C) $C_1 = 0.1$ $(\text{kPa s})^{-1}$ ($\sigma \rightarrow \phi_a$) and $E_c = 0.6$ kPa ($\phi_a \not\rightarrow E_c$); (D) $C_1 = 0.1$ $(\text{kPa s})^{-1}$ ($\sigma \rightarrow \phi_a$) and $E_c = f(\phi_a)$ ($\phi_a \rightarrow E_c$). Within each subfigure, the rows represent ρ_a , ϕ_d , ϕ_a and $|u|$ on a cross-section of the plane $x_1 = 0$ of the axisymmetric cell, and the columns represent $E = 0.1, 5.7, 7 \cdot 10^6$ kPa. Parameter values as in Table 1.

Discussion and Conclusion

We have derived a model for mechanotransduction via the RhoA signalling pathway with ECM stiffness and intracellular mechanical properties serving as the mechanical cues. The modelling extends the work of [18] incorporating the explicit modelling of cell deformation based on an elastic constitutive assumption. We have extended on [18, 23, 24] and introduced a two-way coupling between the mechanics of the cell and biochemical signalling processes. This two-way coupling appears to be central to mechanical homeostasis observed in biological experiments [28]. We propose a robust numerical method, based on the bulk-surface finite element method (FEM), see e.g. [26], for the approximation of the model and report on simulation results for different scenarios, validating the results by com-

parison with simulations presented in [18] and experimental observations in [44]. Namely, we considered different levels of substrate stiffness for cells of different shapes that either sit on a rigid flat substrate or are embedded in a three-dimensional substrate.

Our broad conclusions are that cell shape strongly influences the dynamics of the signalling molecules and the deformation of the cell, as seen in all figures comparing the axisymmetric and lamellipodium shape, where the emergent patterns differ, which is in line with experimental observations [45, 46]. Cell shape also affects experimentally observed features such as the threshold-like response to changes in substrate stiffness [44] which is reproduced by the model. In Fig 3, 5, 7 and in S4 Fig, we see that for certain parameters ($C_1 = 0.1 \text{ (kPa s)}^{-1}$ and low substrate stiffness), the cell shape affects the mean concentrations of the signalling molecules and the mean volume change of the cell, and thus changes the threshold-like response.

Our simulations exhibit novel emergent features, that are inaccessible without the framework we propose, such as the bidirectional coupling between mechanics and signalling processes through allowing the Young's modulus of the cell to depend on protein concentration that can allow for robustness in terms of the magnitude of deformation in response to differences in substrate stiffness. This is an example of a mechanical homeostasis mechanism that emerges only at this level of modelling complexity which is of relevance to biology [28]. Other instances of mechanical homeostasis are the stress being maintained in the cardiovascular system under mechanical perturbations [47] and the tensional homeostasis by the RhoA signalling pathway at the level of multiple cells [48, 49], which is known to be governed by cellular stiffness sensing [50]. Another mechanism that experiences homeostatic response to substrate stiffness is that of the mechanical memory of the cell, describing the phenomenon of a cell responding less to substrates with lower stiffness if they have been cultured on stiff substrates [49, 51]. Due to the bidirectional coupling between the mechanics and the chemistry in our modelling framework, an extension of this work by changing the chosen couplings could be used to model these other mechanical homeostasis phenomena.

Based on previous biological studies [18, 38], we considered cases in which the mechanical properties of the cell (cell stiffness) depend on the concentration of signalling molecules. This coupling yields less sensitivity of total deformation to substrate stiffness whilst leaving the dynamics of the signalling molecules themselves broadly unchanged, see Fig 3, 5, 7 and in S4 Fig. The insensitivity of the dynamics of the signalling molecules to deformation levels arises since in the model proposed here they are influenced by the local stress rather than deformation. We note that the above constitutes another emergent homeostasis mechanism that the modelling framework allows us to explore. We stress that our work serves as an example of how mechanotransduction may be modelled and more complicated models for the mechanics, biochemistry and couplings therefore are warranted based on the remarkable emergent features we observe even in our relatively simple setting. We expect such models to be particularly fruitful avenues for future work.

One such example of more complicated models for the mechanics could include a viscoelastic or poroelastic constitutive law. As presented in Section A.7 in S1 Appendix, the assumption of a (linear) viscoelastic constitutive law leads to qualitatively similar results to those presented in this work for a purely (linear) elastic constitutive law. Our current assumption of a linear elastic constitutive law for the mechanics of the cell is limiting as it assumes small deformations. This framework needs to be extended to study the effect of large deformations and shape changes, which would include the effect these deformations have on the signalling molecules. This would be especially interesting, as this study shows that cell shape is one of the determinants affecting the mean concentrations of the signalling molecules.

The boundary conditions for the deformation we consider correspond to simple models of a cell in vitro (flat 2D substrate) or in vivo (homogeneous 3D matrix). We see that the cell on a 2D substrate appears to spread radially with minimal deformation orthogonal to the substrate while the latter exhibits a more uniform although smaller in total magnitude 3D deformation. Differences in deformation for different environments are in line with the literature as the effect of the substrate stiffness on cells is known to vary in 2D and 3D substrates [52]. An interesting extension that could be included in the above framework would be spatial variations in substrate stiffness or more complicated models for the substrate mechanics both of which are of much biological relevance [53, 54, 55].

This work shows how mechanistic modelling of mechanotransduction can reveal remarkable emergent properties. It lays the groundwork for future studies where further complexity can be added as required to model specific signalling pathways or to reflect other mechanical models derived from different constitutive assumptions. We anticipate that choosing a viscoelastic or poroelastic constitutive law for the mechanics of the cell is an interesting direction for future studies, as this is in line with recent experimental observations [31, 32]. Given the fact that cell shape greatly influences the dynamics of the cell, as shown in this work, other reference geometries are also of interest as a subject for future work. Extending the signalling model of [18] further, we intend to couple the model of this work with a similar biomechanical model for the deformation of the nucleus coupled with the dynamics of signalling molecules within the nucleus, such as the YAP/TAZ pathway [56].

Acknowledgments

SV was supported by the EPSRC Centre for Doctoral Training in Mathematical Modelling, Analysis and Computation (MAC-MIGS) funded by the UK Engineering and Physical Sciences Research Council (grant EP/S023291/1), Heriot-Watt University and the University of Edinburgh. CV acknowledges support from the Dr Perry James (Jim) Browne Research Centre on Mathematics and its Applications (University of Sussex).

SV and MP would like to thank the Isaac Newton Institute for Mathematical Sciences, Cambridge, for support and hospitality during the research programme 'Uncertainty quantification and stochastic modelling of materials', EPSRC Grant Number EP/R014604/1, where some work on the manuscript was undertaken.

The authors would like to thank Padmini Rangamani for helpful discussions.

References

- [1] Tomar A, Lim ST, Lim Y, Schlaepfer DD. A FAK-p120RasGAP-p190RhoGAP complex regulates polarity in migrating cells. *Journal of Cell Science*. 2009;122:1852–1862. doi:10.1242/jcs.046870.
- [2] Valls PO, Esposito A. Signalling dynamics, cell decisions, and homeostatic control in health and disease. *J Cell Sci Curr Opin Cell Biol*. 2022;75:102066. doi:10.1016/j.ceb.2022.01.011.
- [3] Romani P, Valcarcel-Jimenez L, Frezza C, Dupont S. Crosstalk between mechanotransduction and metabolism. *Nature Reviews Molecular Cell Biology*. 2021;22(1):22–38. doi:10.1038/s41580-020-00306-w.
- [4] Cai X, Wang KC, Meng Z. Mechanoregulation of YAP and TAZ in Cellular Homeostasis and Disease Progression. *Front Cell Dev Biol*. 2021;9:673599. doi:10.3389/fcell.2021.673599.
- [5] Humphrey JD, Dufresne ER, Schwartz MA. Mechanotransduction and extracellular matrix homeostasis. *Nature reviews Molecular cell biology*. 2014;15(12):802–812. doi:10.1038/nrm3896.
- [6] Saraswathibhatla A, Indiana D, Chaudhuri O. Cell-extracellular matrix mechanotransduction in 3D. *Nature Reviews Molecular Cell Biology*. 2023;24(7):495–516. doi:10.1038/s41580-023-00583-1.
- [7] Burridge K, Monaghan-Benson E, Graham DM. Mechanotransduction: from the cell surface to the nucleus via RhoA. *Philosophical Transactions of the Royal Society B: Biological Sciences*. 2019;374(1779):20180229. doi:10.1098/rstb.2018.0229.
- [8] Xie N, Xiao C, Shu Q, Cheng B, Wang Z, Xue R, et al. Cell response to mechanical microenvironment cues via Rho signaling: From mechanobiology to mechanomedicine. *Acta Biomaterialia*. 2023;159:1–20. doi:10.1016/j.actbio.2023.01.039.
- [9] Martino F, Perestrelo AR, Vinarský V, Pagliari S, Forte G. Cellular Mechanotransduction: From Tension to Function. *Frontiers in Physiology*. 2018;9.
- [10] Sun Z, Guo SS, Fässler R. Integrin-mediated mechanotransduction. *J Cell Biol*. 2016;215(4):445–456. doi:10.1083/jcb.201609037.
- [11] Young KM, Reinhart-King CA. Environmental stiffness restores mechanical homeostasis in vimentin-depleted cells. *Current Opinion in Cell Biology*. 2023;83:102208. doi:10.1016/j.ceb.2023.102208.
- [12] Gilbert D, Fuss H, Gu X, Orton R, Robinson S, Vyshemirsky V, et al. Computational methodologies for modelling, analysis and simulation of signalling networks. *Briefings in Bioinformatics*. 2006;7(4):339–353. doi:10.1093/bib/bbl043.
- [13] García-Penarrubia P, J J Gálvez JJ, Gálvez J. Mathematical modelling and computational study of two-dimensional and three-dimensional dynamics of receptor–ligand interactions in signalling response mechanisms. *J Math Biol*. 2014;69:553–582.
- [14] Ptashnyk M, Venkataraman C. Multiscale Analysis and Simulation of a Signaling Process With Surface Diffusion. *Multiscale Modeling & Simulation*. 2020;18(2):851–886. doi:10.1137/18M1185661.
- [15] Cheng B, Lin M, Huang G, Li Y, Ji B, Genin GM, et al. Cellular mechanosensing of the biophysical microenvironment: A review of mathematical models of biophysical regulation of cell responses. *Physics of Life Reviews*. 2017;22–23:88–119. doi:10.1016/j.plrev.2017.06.016.

[16] Besser A, Schwarz US. Coupling biochemistry and mechanics in cell adhesion: a model for inhomogeneous stress fiber contraction. *New Journal of Physics*. 2007;9(11):425–425. doi:10.1088/1367-2630/9/11/425.

[17] Novev JK, Heltberg ML, Jensen MH, Doostmohammadi A. Spatiotemporal model of cellular mechanotransduction via Rho and YAP. *Integrative Biology*. 2021;13(8):197–209. doi:10.1093/intbio/zyab012.

[18] Scott KE, Fraley SI, Rangamani P. A spatial model of YAP/TAZ signaling reveals how stiffness, dimensionality, and shape contribute to emergent outcomes. *Proceedings of the National Academy of Sciences*. 2021;118(20):e2021571118. doi:10.1073/pnas.2021571118.

[19] Kang J, Puskar KM, Ehrlicher AJ, LeDuc PR, Schwartz RS. Structurally Governed Cell Mechanotransduction through Multiscale Modeling. *Scientific Reports*. 2015;5(1):8622. doi:10.1038/srep08622.

[20] Bar-Ziv R, Tlusty T, Moses E, Safran SA, Bershadsky A. Pearling in cells: A clue to understanding cell shape. *Proceedings of the National Academy of Sciences*. 1999;96(18):10140–10145. doi:10.1073/pnas.96.18.10140.

[21] Vianay B, Käfer J, Planus E, Block M, Graner F, Guillou H. Single Cells Spreading on a Protein Lattice Adopt an Energy Minimizing Shape. *Physical Review Letters*. 2010;105(12):128101. doi:10.1103/PhysRevLett.105.128101.

[22] Albert PJ, Schwarz US. Dynamics of cell shape and forces on micropatterned substrates predicted by a cellular Potts model. *Biophysical Journal*. 2014;106(11):2340–2352. doi:10.1016/j.bpj.2014.04.036.

[23] Sun M, Spill F, Zaman MH. A Computational Model of YAP/TAZ Mechanosensing. *Biophysical Journal*. 2016;110(11):2540. doi:10.1016/j.bpj.2016.04.040.

[24] Eroumé KS, Cavill R, Staňková K, de Boer J, Carlier A. Exploring the influence of cytosolic and membrane FAK activation on YAP/TAZ nuclear translocation. *Biophysical Journal*. 2021;120(20):4360–4377. doi:10.1016/j.bpj.2021.09.009.

[25] Gould PL. *Introduction to Linear Elasticity*. Springer New York; 2013. Available from: <http://link.springer.com/10.1007/978-1-4614-4833-4>.

[26] Dziuk G, Elliott CM. Finite element methods for surface PDEs. *Acta Numerica*. 2013;22:289–396. doi:10.1017/S0962492913000056.

[27] Gilbert PM, Weaver VM. Cellular adaptation to biomechanical stress across length scales in tissue homeostasis and disease. *Seminars Cell Develop Biol*. 2017;67:141–152. doi:10.1016/j.semcdedb.2016.09.004.

[28] Grolleman J, van Engeland NCA, Raza M, Azimi S, Conte V, Sahlgren CM, et al. Environmental stiffness restores mechanical homeostasis in vimentin-depleted cells. *Nature, Scientific Reports*. 2023;13:18374. doi:10.1038/s41598-023-44835-8.

[29] McNicol GR, Dalby MJ, Stewart PS. A theoretical model for focal adhesion and cytoskeleton formation in non-motile cells. *Journal of Theoretical Biology*. 2025;596:111965. doi:10.1016/j.jtbi.2024.111965.

[30] Di X, Gao X, Peng L, Ai J, Jin X, Qi S, et al. Cellular mechanotransduction in health and diseases: from molecular mechanism to therapeutic targets. *Sig Transduct Target Ther*. 2023;8:282. doi:10.1038/s41392-023-01501-9.

[31] Kasza KE, Rowat AC, Liu J, Angelini TE, Brangwynne CP, Koenderink GH, et al. The cell as a material. *Current Opinion in Cell Biology*. 2007;19(1):101–107. doi:10.1016/j.ceb.2006.12.002.

[32] Moeendarbary E, Valon L, Fritzsch M, Harris AR, Moulding DA, Thrasher AJ, et al. The cytoplasm of living cells behaves as a poroelastic material. *Nature Materials*. 2013;12(3):253–261. doi:10.1038/nmat3517.

[33] Banerjee S, Marchetti MC. Controlling cell–matrix traction forces by extracellular geometry. *New Journal of Physics*. 2013;15(3):035015. doi:10.1088/1367-2630/15/3/035015.

[34] Oakes PW, Banerjee S, Marchetti MC, Gardel ML. Geometry Regulates Traction Stresses in Adherent Cells. *Biophysical Journal*. 2014;107(4):825–833. doi:10.1016/j.bpj.2014.06.045.

[35] Chojowski R, Schwarz US, Ziebert F. Reversible elastic phase field approach and application to cell monolayers. *The European Physical Journal E*. 2020;43(10):63. doi:10.1140/epje/i2020-11988-1.

[36] Cheng B, Li M, Wan W, Guo H, Genin GM, Lin M, et al. Predicting YAP/TAZ Nuclear Translocation in Response to ECM Mechanosensing. *Biophysical Journal*. 2023;122(1):43–53. doi:10.1016/j.bpj.2022.11.2943.

[37] Graham DM, Burridge K. Mechanotransduction and nuclear function. *Current Opinion in Cell Biology*. 2016;40:98–105. doi:10.1016/j.ceb.2016.03.006.

[38] Gardel ML, Shin JH, MacKintosh FC, Mahadevan L, Matsudaira P, Weitz DA. Elastic Behavior of Cross-Linked and Bundled Actin Networks. *Science*. 2004;304(5675):1301–1305. doi:10.1126/science.1095087.

[39] Burridge K, Guilluy C. Focal adhesions, stress fibers and mechanical tension. *Experimental Cell Research*. 2016;343:14–20. doi:10.1016/j.yexcr.2015.10.029.

[40] Doyle AD, Carvajal N, Jin A, Matsumoto K, Yamada KM. Local 3D matrix microenvironment regulates cell migration through spatiotemporal dynamics of contractility-dependent adhesions. *J Cell Sci*. 2015;6:8720. doi:10.1038/ncomms9720.

[41] Zhao XH, Laschinger C, Arora P, Szászki K, Kapus A, McCulloch CA. Force activates smooth muscle α -actin promoter activity through the Rho signaling pathway. *J Cell Sci*. 2007;120:1801–1809. doi:10.1242/jcs.001586.

[42] Mokbel M, Hosseini K, Aland S, Fischer-Friedrich E. The Poisson Ratio of the Cellular Actin Cortex Is Frequency Dependent. *Biophysical Journal*. 2020;118(8):1968–1976. doi:10.1016/j.bpj.2020.03.002.

[43] Chrzanowska-Wodnicka M, Burridge K. Rho-stimulated contractility drives the formation of stress fibers and focal adhesions. *Journal of Cell Biology*. 1996;133(6):1403–1415. doi:10.1083/jcb.133.6.1403.

[44] Beamish JA, Chen E, Putnam AJ. Engineered extracellular matrices with controlled mechanics modulate renal proximal tubular cell epithelialization. *PLOS ONE*. 2017;12(7):e0181085. doi:10.1371/journal.pone.0181085.

[45] Chen CS, Alonso JL, Ostuni E, Whitesides GM, Ingber DE. Cell shape provides global control of focal adhesion assembly. *Biochemical and Biophysical Research Communications*. 2003;307(2):355–361. doi:10.1016/S0006-291X(03)01165-3.

[46] McBeath R, Pirone DM, Nelson CM, Bhadriraju K, Chen CS. Cell Shape, Cytoskeletal Tension, and RhoA Regulate Stem Cell Lineage Commitment. *Developmental Cell*. 2004;6(4):483–495. doi:10.1016/S1534-5807(04)00075-9.

[47] Kassab GS. Biomechanical Homeostasis. In: Kassab GS, editor. *Coronary Circulation: Mechanobiology, Growth, Remodeling, and Clinical Implications*. Cham: Springer International Publishing; 2024. p. 1–43. Available from: https://doi.org/10.1007/978-3-031-62652-4_1.

[48] Andersen T, Wörthmüller D, Probst D, Wang I, Moreau P, Fitzpatrick V, et al. Cell size and actin architecture determine force generation in optogenetically activated cells. *Biophysical Journal*. 2023;122(4):684–696. doi:10.1016/j.bpj.2023.01.011.

[49] Weaver VM, Gilbert PM. Cellular adaptation to biomechanical stress across length scales in tissue homeostasis and disease. *Seminars in cell & developmental biology*. 2016;67:141. doi:10.1016/j.semcdb.2016.09.004.

[50] Chanduri M, Kumar A, Weiss D, Emuna N, Barsukov I, Shi M, et al. Cellular stiffness sensing through talin 1 in tissue mechanical homeostasis. *Science Advances*. 2024;10(34):eadi6286. doi:10.1126/sciadv.adi6286.

[51] Cacopardo L, Guazzelli N, Ahluwalia A. Characterizing and Engineering Biomimetic Materials for Viscoelastic Mechanotransduction Studies. *Tissue Engineering Part B, Reviews*. 2022;28(4):912–925. doi:10.1089/ten.TEB.2021.0151.

[52] Byfield FJ, Reen RK, Shentu TP, Levitan I, Gooch KJ. Endothelial actin and cell stiffness is modulated by substrate stiffness in 2D and 3D. *Journal of Biomechanics*. 2009;42(8):1114–1119. doi:10.1016/j.jbiomech.2009.02.012.

[53] Chaudhuri O, Gu L, Darnell M, Klumpers D, Bencherif SA, Weaver JC, et al. Substrate stress relaxation regulates cell spreading. *Nature Communications*. 2015;6(1):6365. doi:10.1038/ncomms7365.

[54] Isomursu A, Park K-Y, Hou J, Cheng B, Mathieu M, Shamsan GA, et al. Directed Cell Migration towards Softer Environments. *Nature Materials*. 2022;21(9):1081–1090. doi:10.1038/s41563-022-01294-2.

- [55] Ross AM, Jiang Z, Bastmeyer M, Lahann J. Physical Aspects of Cell Culture Substrates: Topography, Roughness, and Elasticity. *Small*. 2012;8(3):336–355. doi:10.1002/smll.201100934.
- [56] Jafarinia H, Khalilimeybodi A, Barrasa-Fano J, Fraley SI, Rangamani P, Carlier A. Insights gained from computational modeling of YAP/TAZ signaling for cellular mechanotransduction. *npj Systems Biology and Applications*. 2024;10(1):1–14. doi:10.1038/s41540-024-00414-9.
- [57] Le Dévédec SE, Geverts B, de Bont H, Yan K, Verbeek FJ, Houtsmuller AB, et al. The residence time of focal adhesion kinase (FAK) and paxillin at focal adhesions in renal epithelial cells is determined by adhesion size, strength and life cycle status. *Journal of Cell Science*. 2012;125:4498–4506. doi:10.1242/jcs.104273.
- [58] Logg A, Mardal KA, Wells G, editors. Automated Solution of Differential Equations by the Finite Element Method. vol. 84 of Lecture Notes in Computational Science and Engineering. Berlin, Heidelberg: Springer Berlin Heidelberg; 2012. Available from: <http://link.springer.com/10.1007/978-3-642-23099-8>.
- [59] Geuzaine C, Remacle JF. Gmsh: A 3-D finite element mesh generator with built-in pre- and post-processing facilities. *International Journal for Numerical Methods in Engineering*. 2009;79(11):1309–1331. doi:10.1002/nme.2579.
- [60] Lakkis O, Madzvamuse A, Venkataraman C. Implicit-explicit timestepping with finite element approximation of reaction-diffusion systems on evolving domains. *SIAM Journal on Numerical Analysis*. 2013;51(4):2309–2330. doi:10.1137/120880112.

S1 Fig

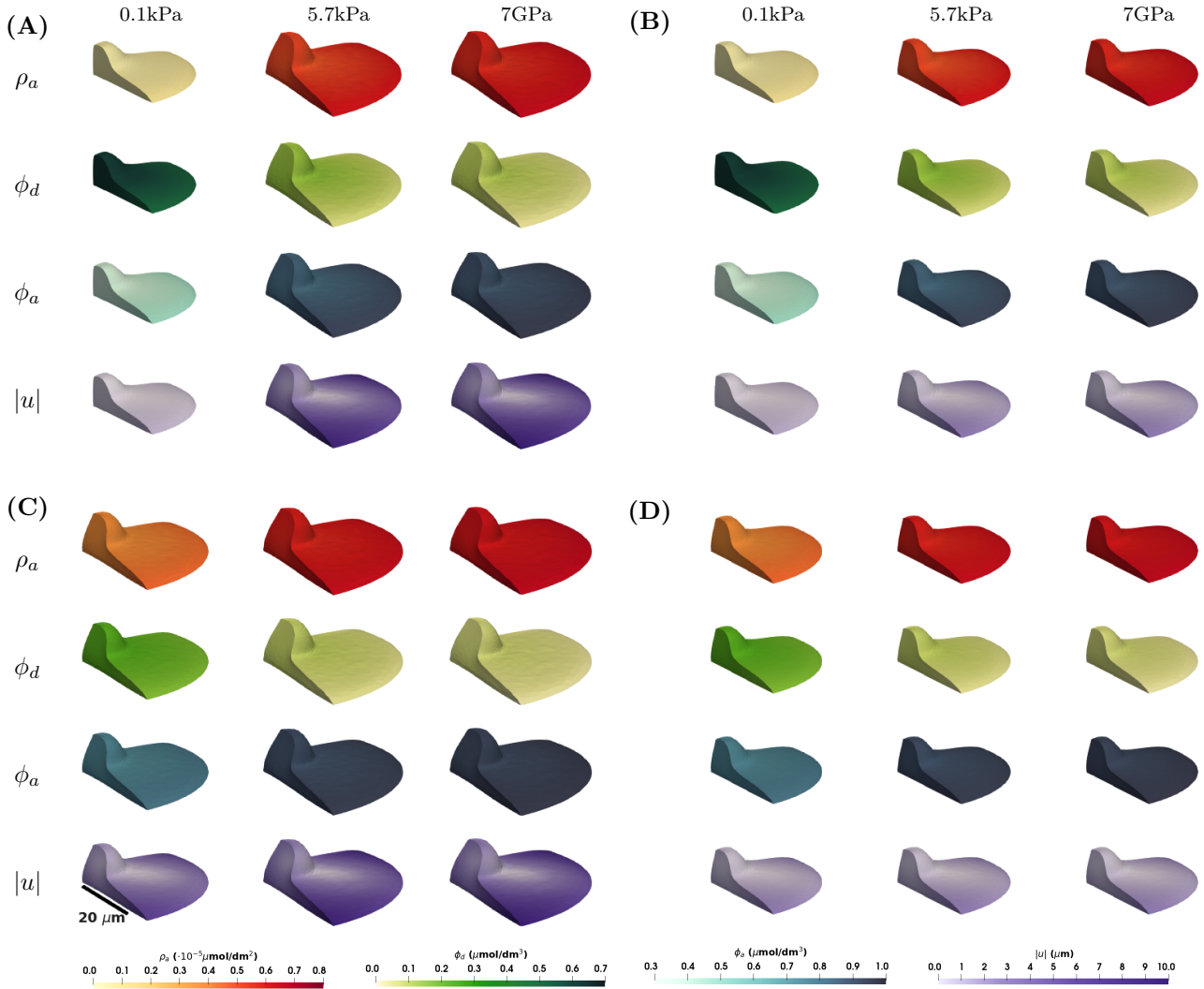


Figure 9: **Numerical simulation results showing ρ_a , ϕ_d , ϕ_a and $|u|$ for the model in Eqs (3)-(6) for the lamellipodium shape and in the case of the 3D stimulus at a steady state at $T = 100$ s.** Four different scenarios are considered: **(A)** $C_1 = 0 \text{ (kPa s)}^{-1}$ ($\sigma \not\rightarrow \phi_a$) and $E_c = 0.6 \text{ kPa}$ ($\phi_a \not\rightarrow E_c$); **(B)** $C_1 = 0 \text{ (kPa s)}^{-1}$ ($\sigma \not\rightarrow \phi_a$) and $E_c = f(\phi_a)$ ($\phi_a \rightarrow E_c$); **(C)** $C_1 = 0.1 \text{ (kPa s)}^{-1}$ ($\sigma \rightarrow \phi_a$) and $E_c = 0.6 \text{ kPa}$ ($\phi_a \not\rightarrow E_c$); **(D)** $C_1 = 0.1 \text{ (kPa s)}^{-1}$ ($\sigma \rightarrow \phi_a$) and $E_c = f(\phi_a)$ ($\phi_a \rightarrow E_c$). Within each subfigure, the rows represent ρ_a , ϕ_d , ϕ_a and $|u|$ on the surface of the cell, and the columns represent $E = 0.1, 5.7, 7 \cdot 10^6 \text{ kPa}$. Parameter values as in Table 1.

S2 Fig

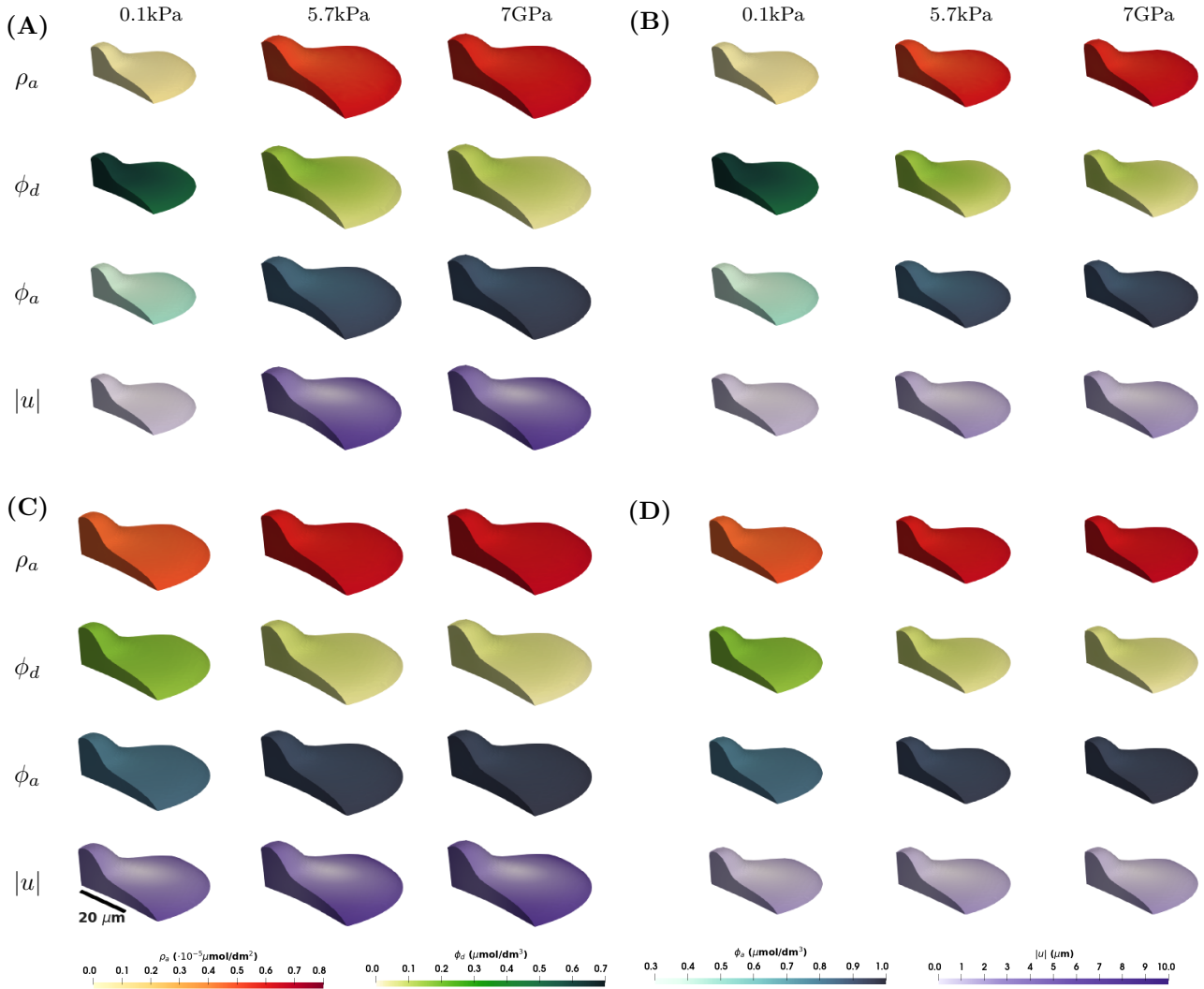


Figure 10: Numerical simulation results showing ρ_a , ϕ_d , ϕ_a and $|u|$ for the model in Eqs (3), (4), and (6) for the lamellipodium shape and in the case of the 3D stimulus at a steady state at $T = 100$ s. Four different scenarios are considered: (A) $C_1 = 0$ $(\text{kPa s})^{-1}$ ($\sigma \not\rightarrow \phi_a$) and $E_c = 0.6$ kPa ($\phi_a \not\rightarrow E_c$); (B) $C_1 = 0$ $(\text{kPa s})^{-1}$ ($\sigma \not\rightarrow \phi_a$) and $E_c = f(\phi_a)$ ($\phi_a \rightarrow E_c$); (C) $C_1 = 0.1$ $(\text{kPa s})^{-1}$ ($\sigma \rightarrow \phi_a$) and $E_c = 0.6$ kPa ($\phi_a \not\rightarrow E_c$); (D) $C_1 = 0.1$ $(\text{kPa s})^{-1}$ ($\sigma \rightarrow \phi_a$) and $E_c = f(\phi_a)$ ($\phi_a \rightarrow E_c$). Within each subfigure, the rows represent ρ_a , ϕ_d , ϕ_a and $|u|$ on the surface of the cell, and the columns represent $E = 0.1, 5.7, 7 \cdot 10^6$ kPa. Parameter values as in Table 1.

S3 Fig

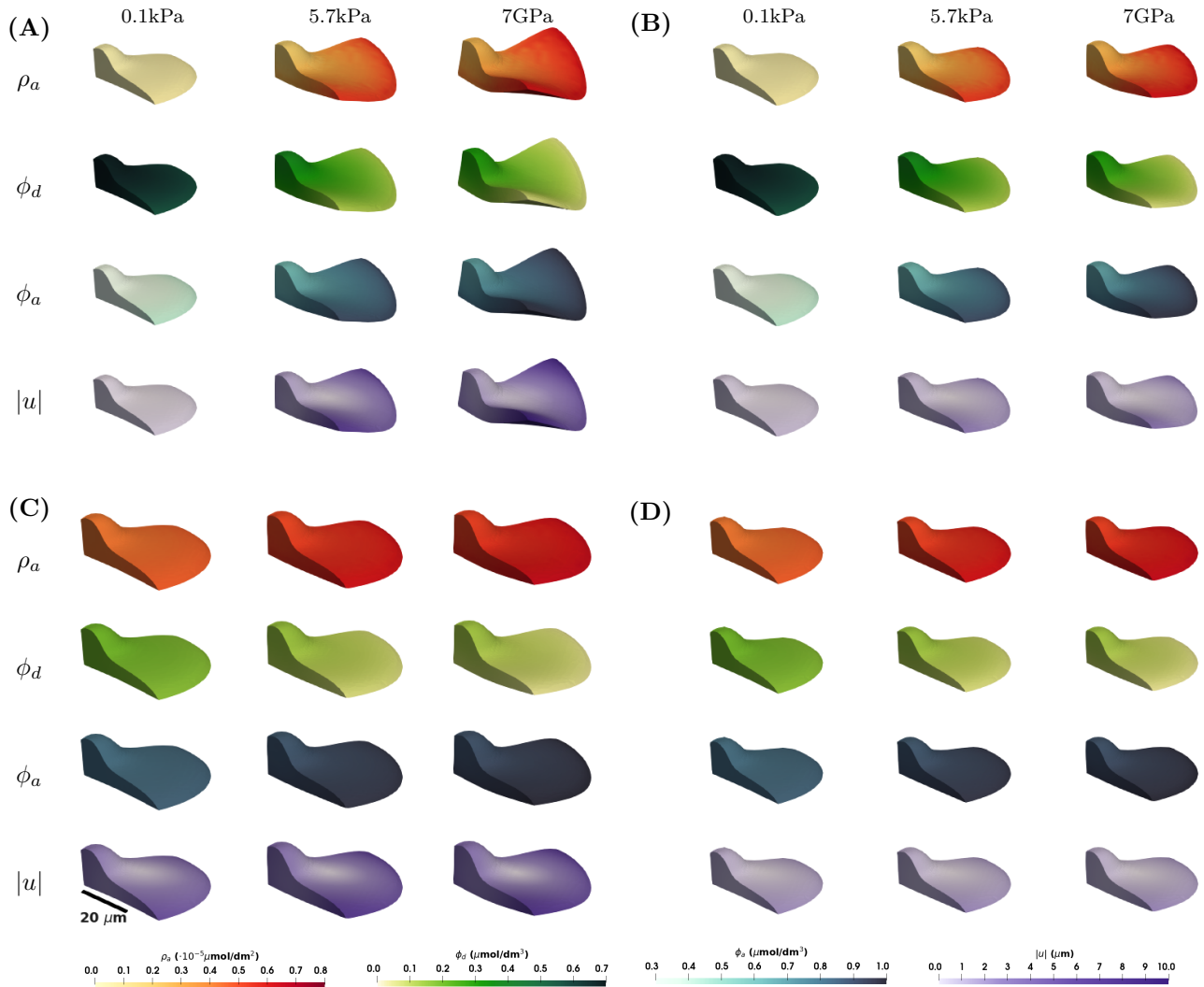


Figure 11: Numerical simulation results showing ρ_a , ϕ_d , ϕ_a and $|u|$ for the model in Eqs (3), (4), and (6) for the lamellipodium shape cells and 2xD stimulus at a steady state at $T = 100$ s. Four different scenarios are considered: (A) $C_1 = 0$ $(\text{kPa s})^{-1}$ ($\sigma \not\rightarrow \phi_a$) and $E_c = 0.6$ kPa ($\phi_a \not\rightarrow E_c$); (B) $C_1 = 0$ $(\text{kPa s})^{-1}$ ($\sigma \not\rightarrow \phi_a$) and $E_c = f(\phi_a)$ ($\phi_a \rightarrow E_c$); (C) $C_1 = 0.1$ $(\text{kPa s})^{-1}$ ($\sigma \rightarrow \phi_a$) and $E_c = 0.6$ kPa ($\phi_a \not\rightarrow E_c$); (D) $C_1 = 0.1$ $(\text{kPa s})^{-1}$ ($\sigma \rightarrow \phi_a$) and $E_c = f(\phi_a)$ ($\phi_a \rightarrow E_c$). Within each subfigure, the rows represent ρ_a , ϕ_d , ϕ_a and $|u|$ on the surface of the cell, and the columns represent $E = 0.1, 5.7, 7 \cdot 10^6$ kPa. Parameter values as in Table 1.

S4 Fig

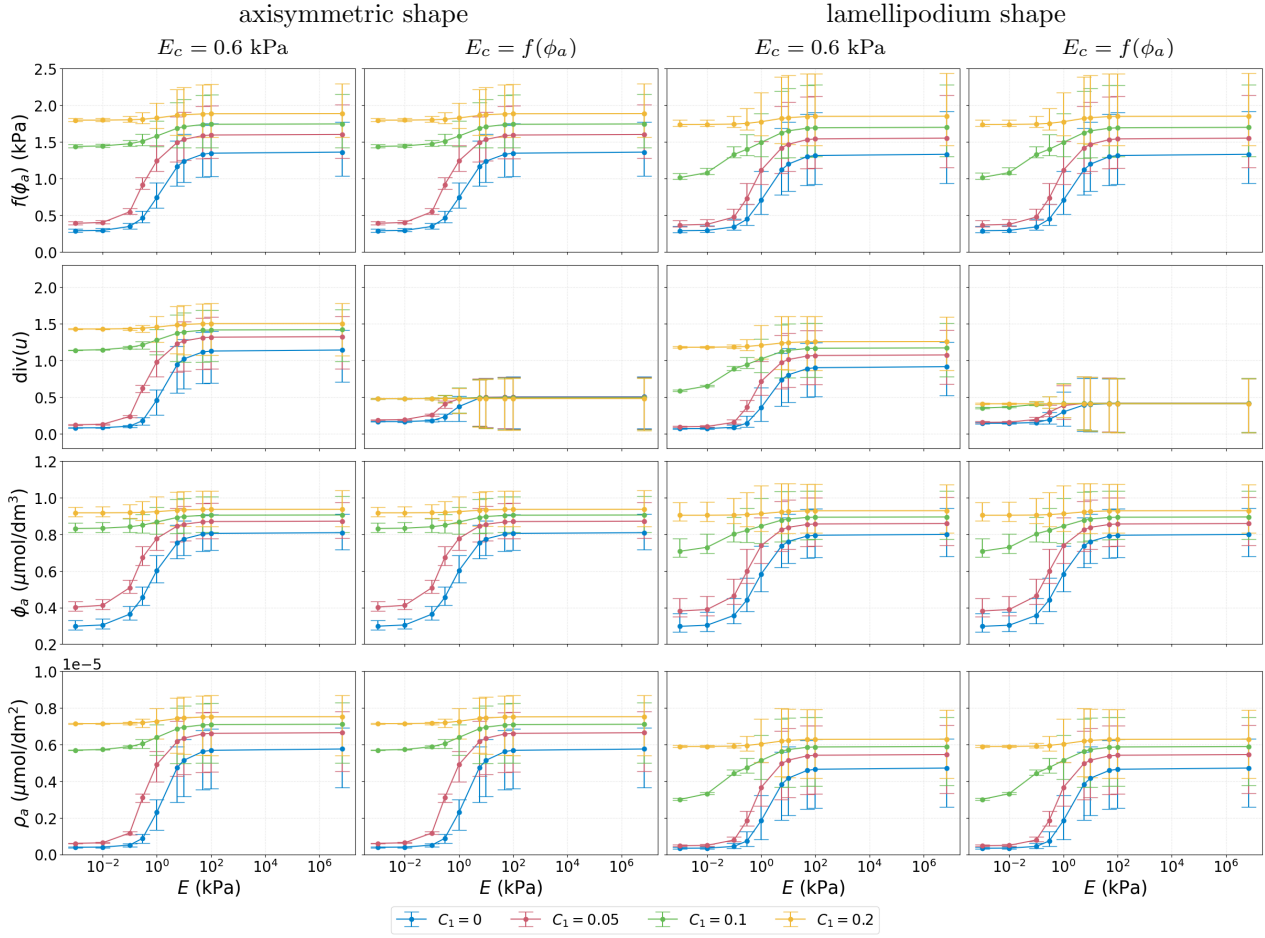


Figure 12: **Simulation results showing the mean, $\frac{1}{|\Omega|} \int_{\Omega} \cdot \, dx$, min and max values of $f(\phi_a)$, $\text{div}(u)$, ϕ_a and ρ_a as functions of substrate stiffness E , in the case of the model in Eqs (3), (4) and (6) and 2x1D stimulus.** We consider different couplings, four different values for C_1 , and two different shapes at $T = 100$ s by which time the results are at a steady state. All other parameter values as in Table 1.

S1 Appendix

A.1 Comparison of the reduced model and the full model of [18]

We verify the reduced model (1) captures the results obtained in [18] for the full model for the RhoA signalling pathway. In numerical simulations of model (1) we use the same parameter values as in [18], except for the diffusion coefficients D_1 and D_2 for activated and deactivated FAK. It is suggested in the literature that $D_1 = D_2 = 4 \mu\text{m}^2/\text{s}$ [57], but [18] uses $10 \mu\text{m}^2/\text{s}$ due to computational issues. Thus in our numerical simulations we consider both diffusion coefficients.

$\phi_d^0 = 0.7 \mu\text{mol}/\text{dm}^3$	$C = 3.25 \text{ kPa}$	$D_1 = 4 \text{ or } 10 \mu\text{m}^2/\text{s}$	$k_2 = 0.015 \text{ s}^{-1}$
$\phi_a^0 = 0.3 \mu\text{mol}/\text{dm}^3$	$\gamma = 8.8068 \text{ dm}^3/\mu\text{mol}$	$D_2 = 4 \text{ or } 10 \mu\text{m}^2/\text{s}$	$k_3 = 0.379 \text{ s}^{-1}$
$\rho_a^0 = 33.6 \#/\mu\text{m}^2$	$n = 5$	$D_3 = 0.3 \mu\text{m}^2/\text{s}$	$k_4 = 0.625 \text{ s}^{-1}$
$\approx 6 \cdot 10^{-7} \mu\text{mol}/\text{dm}^2$	$E = 0.1, 5.7, 7 \cdot 10^6 \text{ kPa}$	$k_1 = 0.035 \text{ s}^{-1}$	$k_5 = 0.0168 \text{ s}^{-1}$
$\rho_d^0 = 1 \mu\text{mol}/\text{dm}^3$	$ Y = 1193 \mu\text{m}^3$	$ \Gamma = 1020 \mu\text{m}^2$	

Table A1: Parameter values for model (1).

The model (1) is implemented in FEniCS [58], using a Finite Element Method for discretization in space and IMEX time-stepping method to discretize in time, see Section A.3 for more details. Considering domain $Y \subset \mathbb{R}^3$, denoting the cytoplasm, and $\Gamma = \partial Y$, defining the cell membrane, and times interval $(0, T)$, with $T = 100 \text{ s}$, for the space discretisation we choose meshsize $h = 2.94$ and time step $\Delta t = 0.5$ for the backwards Euler discretisation in time. For our domain we have $n_r = |Y|/|\Gamma| = 1.17 \mu\text{m}$. We consider three different stimuli, similar to [18], (i) the ‘2D stimulus’, where the substrate stiffness is only applied to the bottom of the cell and any reaction terms of RhoA are nonzero only at the bottom of the cell, (ii) the ‘2xD stimulus’, where the substrate stiffness is only applied to the bottom of the cell but the reaction terms of RhoA are nonzero on the whole cell membrane, and (iii) the ‘3D stimulus’ where the cell is embedded in an agar (substrate) and the impact of the substrate stiffness on the signalling processes is considered on the whole cell membrane.

Comparing the simulation results for reduced model (1) in Figs A1 and A2 to the results presented in [18, Fig 3] for the full model, the dynamics of FAK and RhoA are almost identical qualitatively. Similar to the results in [18, Fig 3], the highest concentration of both ϕ_a and ρ_a is at the edges of the cell. Also, there is threshold value of $E \approx 1 \text{kPa}$, below which the concentrations of ϕ_a and ρ_a stay close to the initial values and then reaches high steady states values, similar for both $E = 5.7 \text{kPa}$ and $E = 7 \text{GPa}$. Quantitatively, the values for ϕ_a are also close to the one reported in [18, Fig 3]. This suggests that the reduction of the model as well as considering the whole cell domain without excluding a nucleus does not have significant effect on the dynamics of FAK. However, for ρ_a we obtain slightly lower concentration, where the maximum concentration in our results is $420 \#/\mu\text{m}^2$ and the maximum concentration in [18, Fig.3] is $593 \#/\mu\text{m}^2$. This difference could be related to the model reduction and approximation for the deactivated RhoA. The differences in the conversion from $\mu\text{mol}/\text{dm}^2$ to $\#/\mu\text{m}^2$ using our approach, see Section A.4 for details, and the approach of [18] may also contribute.

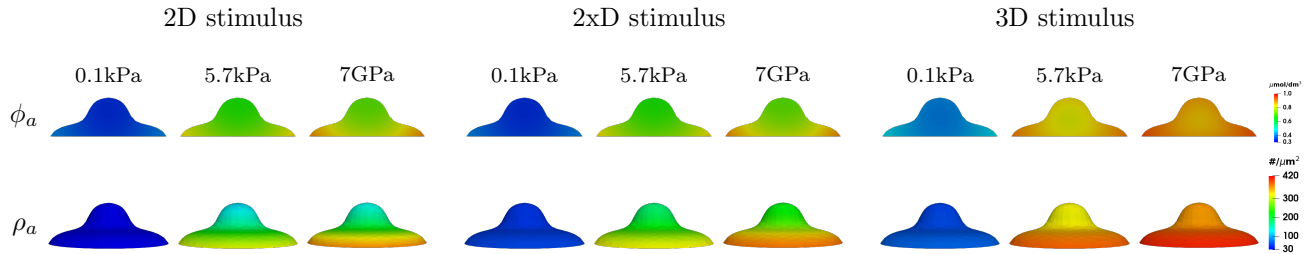


Figure A1: Numerical simulation results showing ϕ_a and ρ_a for reduced model (1) at steady state for $T = 100 \text{ s}$. Parameter values as in Table A1 and $D_1 = D_2 = 4 \mu\text{m}^2/\text{s}$.

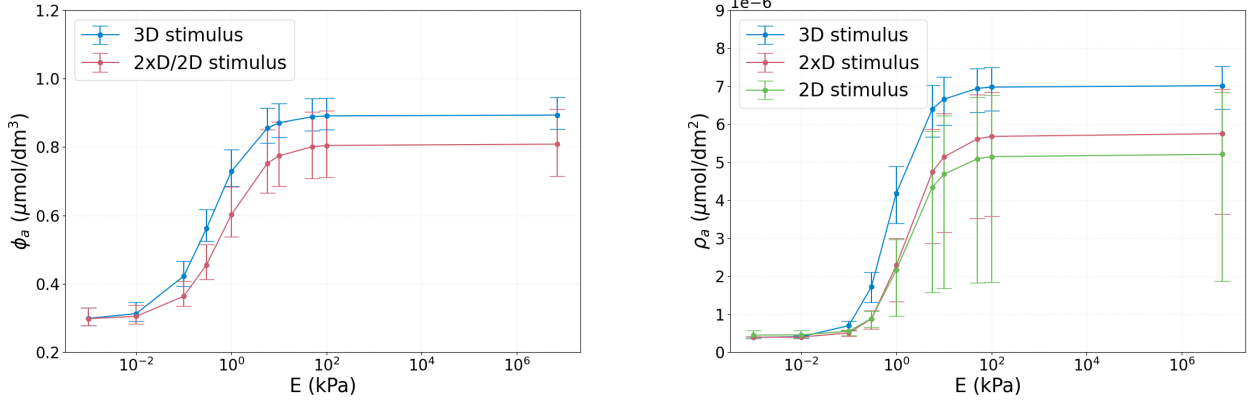


Figure A2: Results showing the effect of substrate stiffness E on ϕ_a and ρ_a for the reduced model (1) at $T = 100$ s by which time the results are at a steady state. Parameter values as in Table A1 with $D_1 = D_2 = 4 \mu\text{m}^2/\text{s}$.

Simulation results for the reduced model with diffusion coefficients $D_1 = D_2 = 10 \mu\text{m}^2/\text{s}$ are presented in Figs A3 and A4. Comparing Figs A2 and A4, we see that the averaged over space dynamics are very similar, but numerical simulation results for a lower diffusion coefficient show lower minimum and higher maximum concentrations, which can be explained by the fact that slower diffusion of ϕ_a causes stronger heterogeneity across the cell domain. In Figs A1 and A3, we observe the same dynamics for both diffusion coefficients, where the maximum concentration is at the edges of the cell and the minimum concentration is in the middle. Since the dynamics of ρ_a depends on ϕ_a , similar results are obtained for ρ_a .

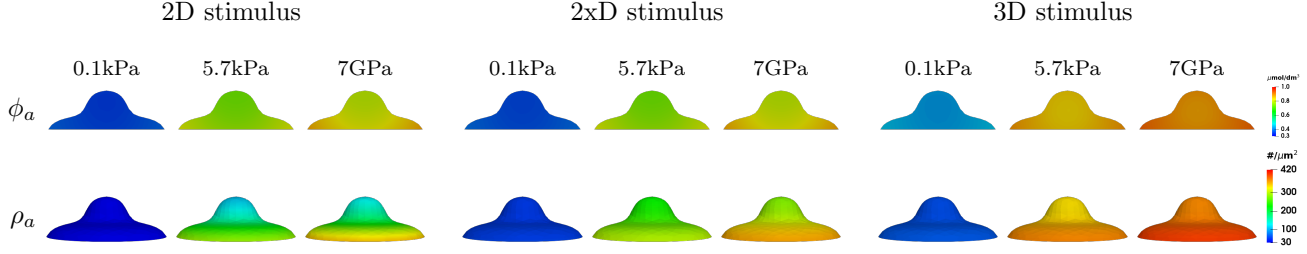


Figure A3: Numerical simulation results showing ϕ_a and ρ_a for reduced model (1) at $T = 100$ s by which time the results are at a steady state. Parameter values as in Table A1 with $D_1 = D_2 = 10 \mu\text{m}/\text{s}$.

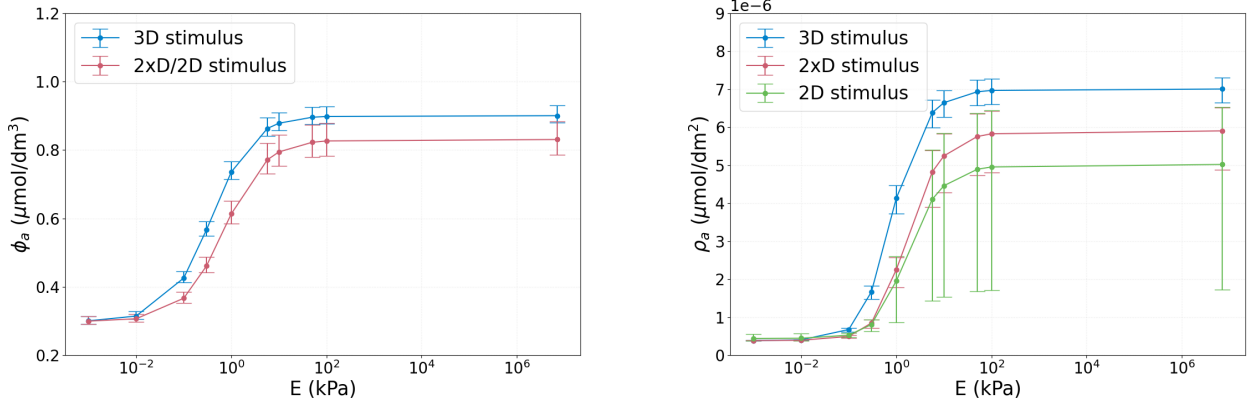


Figure A4: Results showing effect of substrate stiffness E on ϕ_a and ρ_a for the reduced model (1) at $T = 100$ s by which time the results are at a steady state. Parameter values as in Table A1 with $D_1 = D_2 = 10 \mu\text{m}/\text{s}$.

A.2 Temporal statistics

Fig A5 shows the evolution of the mean of $f(\phi_a)$, $\text{div}(u)$, ϕ_a and ρ_a over time for different couplings and parameters for the axisymmetric cell shape.

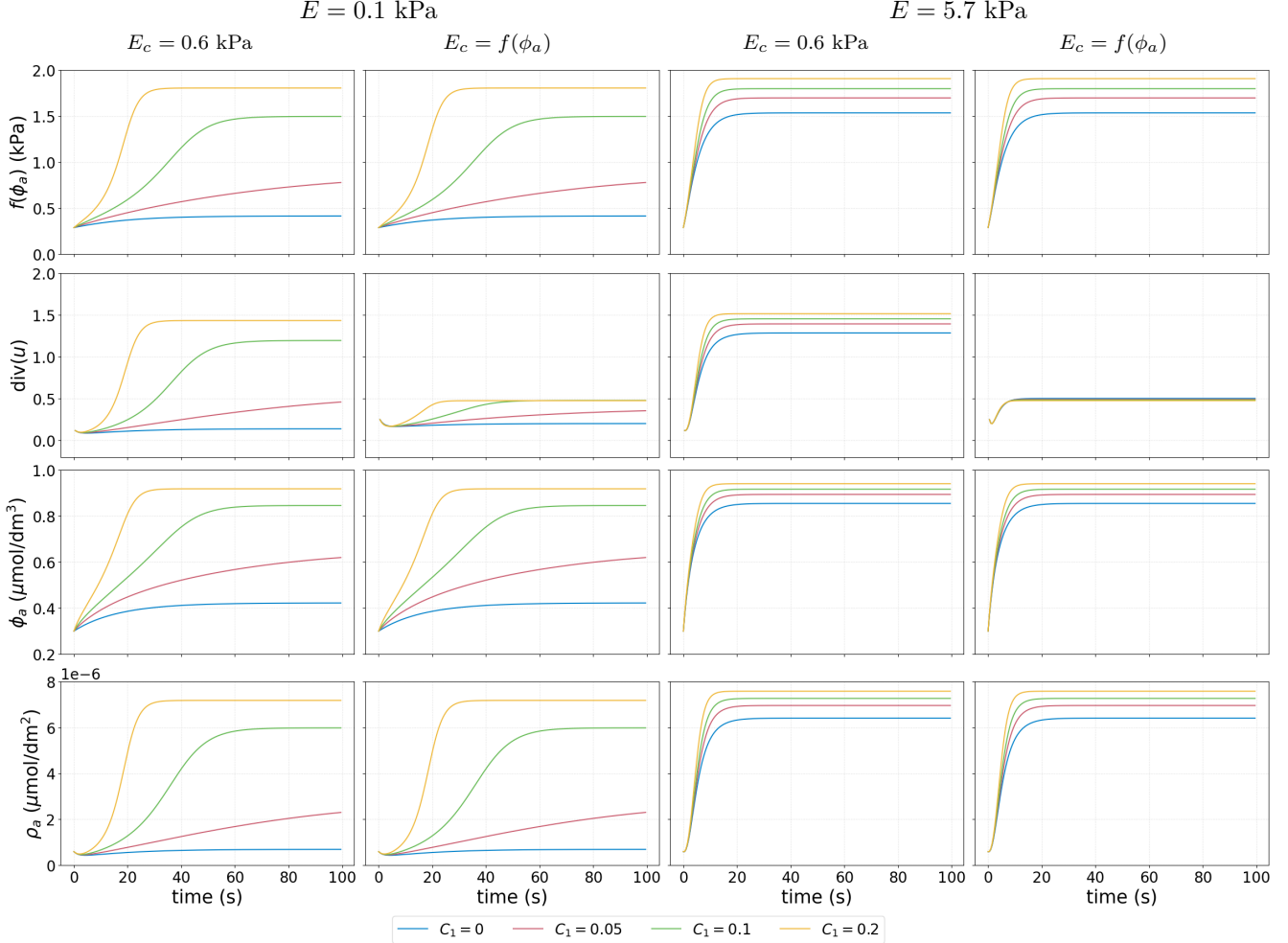


Figure A5: Simulations results showing the mean of $f(\phi_a)$, $\text{div}(u)$, ϕ_a and ρ_a as functions of time, in the case of model (3), (4) and (6), axisymmetric shape and 3D stimulus, for different values for C_1 , and two different values for the substrate stiffness E . All other parameter values as in Table 1. The corresponding results can be found in Fig 6.

A.3 Numerical Scheme

For numerical simulations of model (3)-(6) we use FEM for discretization in space and backward Euler for discretization in time, implemented in FEniCS [58]. Consider the space

$$\mathcal{W}(Y) = \{u \in H^1(Y) : \int_Y u_i \, dx = 0, \int_Y (\partial_{x_j} u_i - \partial_{x_i} u_j) \, dx = 0 \text{ for } i, j = 1, 2, 3\}, \quad (\text{A1})$$

such that $\mathcal{W}(Y) \cap \mathcal{R}(Y) = 0$ with $\mathcal{R}(Y)$ the space of rigid motions. Then, the weak solution of the model (3)-(6) is given by $(\phi_d, \phi_a) \in L^2(0, T; H^1(Y))$, $\rho_a \in L^2(0, T; H^1(\Gamma))$, with $(\partial_t \phi_d, \partial_t \phi_a) \in L^2(0, T; H^1(Y)')$ and

$\partial_t \rho_a \in L^2(0, T; H^1(\Gamma)')$, and $u \in L^2(0, T; \mathcal{W}(Y))$ satisfying

$$\begin{aligned} & \langle \partial_t \phi_d, \psi \rangle_{(H^1)', T} + \langle D_1 \nabla \phi_d, \nabla \psi \rangle_{Y_T} + \langle C_1 \operatorname{tr}(\sigma(u))_+ \phi_d, \psi \rangle_{Y_T} + \langle n_r \tilde{k}_3 \phi_d, \psi \rangle_{\Gamma_T} = \langle k_1 \phi_a, \psi \rangle_{Y_T}, \\ & \langle \partial_t \phi_a, \varphi \rangle_{(H^1)', T} + \langle D_2 \nabla \phi_a, \nabla \varphi \rangle_{Y_T} + \langle k_1 \phi_a, \varphi \rangle_{Y_T} = \langle C_1 \operatorname{tr}(\sigma(u))_+ \phi_d, \varphi \rangle_{Y_T} + \langle n_r \tilde{k}_3 \phi_d, \psi \rangle_{\Gamma_T}, \\ & \langle \partial_t \rho_a, w \rangle_{(H^1)', T} + \langle D_3 \nabla \rho_a, \nabla w \rangle_{\Gamma_T} + \langle \tilde{k}_4(\phi_a) \rho_a, w \rangle_{\Gamma_T} = \langle n_r \tilde{k}_5(\phi_a), w \rangle_{\Gamma_T}, \\ & \langle E(\phi_a) \epsilon(u), \epsilon(v) \rangle_{Y_T} = \langle k_6 \mathbb{P}(\rho_a \nu), v \rangle_{\Gamma_T}, \end{aligned} \quad (\text{A2})$$

for all $\psi, \varphi \in L^2(0, T; H^1(Y))$, $w \in L^2(0, T; H^1(\Gamma))$, and $v \in L^2(0, T; H^1(Y))$, with initial conditions satisfied in the L^2 -sense, and where $\tilde{k}_3 = k_2 + k_3 \frac{E}{C+E}$, $\tilde{k}_4(\phi_a) = k_4 + k_5((\gamma \phi_a)^n + 1)$ and $\tilde{k}_5(\phi_a) = k_5((\gamma \phi_a)^n + 1) \frac{M_\rho}{|Y|}$. Here $\langle \phi, \psi \rangle_{(H^1)', T}$ denotes the dual product between $\phi \in L^2(0, T; H^1(Y))$ and $\psi \in L^2(0, T; H^1(Y)')$ or between $\phi \in L^2(0, T; H^1(\Gamma))$ and $\psi \in L^2(0, T; H^1(\Gamma)')$ and

$$\langle \phi, \psi \rangle_{Y_T} = \int_0^T \int_Y \phi \psi dx dt, \quad \langle \phi_1, \psi_1 \rangle_{\Gamma_T} = \int_0^T \int_{\Gamma} \phi_1 \psi_1 dx dt, \quad \text{where } 1/p_1 + 1/p_2 = 1, \quad 1/q_1 + 1/q_2 = 1,$$

for $\phi \in L^{p_1}(0, T; L^{q_1}(Y))$, $\psi \in L^{p_2}(0, T; L^{q_2}(Y))$, $\phi_1 \in L^{p_1}(0, T; L^{q_1}(\Gamma))$, and $\psi_1 \in L^{p_2}(0, T; L^{q_2}(\Gamma))$. The discretization of the domain is given by the polyhedral approximation of Y such that Y_h is the union of finitely many tetrahedrons in \mathbb{R}^3 , and S_h is the set of these tetrahedrons K , such that

$$Y_h = \bigcup_{K \in S_h} K.$$

Then the surface Γ is approximated by Γ_h such that $\Gamma_h = \partial Y_h$. The mesh size is defined by the maximum diameter of a simplex $h = \max\{h_Y, h_{\Gamma}\}$, where $h_Y = \max_{K \in S_h} h_Y(K)$ and $h_{\Gamma} = \max_{R=K \cap \Gamma_h \neq 0, K \in S_h} h_{\Gamma}(R)$ with $h_Y(K)$ being the diameter of a tetrahedron and $h_{\Gamma}(R)$ the diameter of a triangle on the surface.

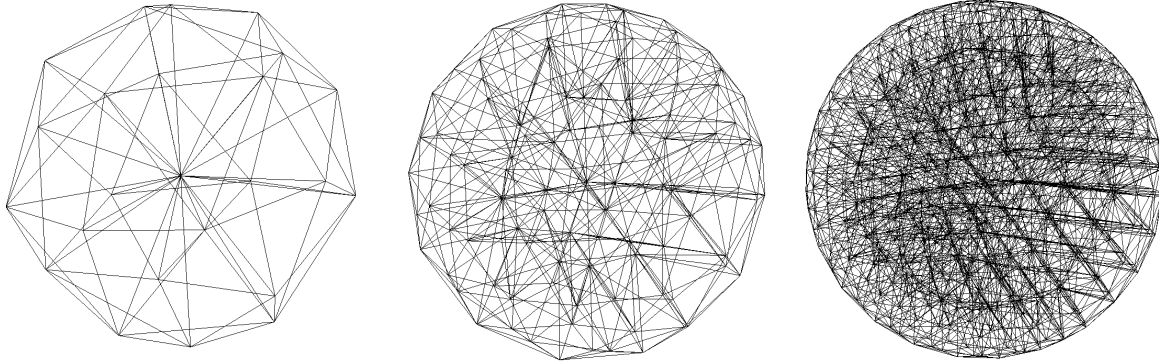


Figure A6: Tetrahedral approximations of a unit sphere with, from left to right, decreasing values of h , created with Gmsh [59].

The bulk and surface finite element spaces are given by

$$\begin{aligned} \mathbb{V}_{h,Y} &= \{\Psi \in C(Y_h) : \Psi|_K \text{ is linear affine for each } K \in S_h\}, \\ \mathbb{V}_{h,\Gamma} &= \{\Psi \in C(\Gamma_h) : \Psi|_R \text{ is linear affine for each } K \in S_h \text{ with } R = K \cap \Gamma_h \neq 0\}, \\ \mathbb{W}_{h,Y} &= \{V \in \mathcal{W}(Y_h) \text{ and } V_i \in C(Y_h) : V_i|_K \text{ is linear affine for each } K \in S_h \text{ for } i = 1, 2, 3\}, \end{aligned}$$

where we recall the definition of \mathcal{W} in Eq (A1). The bulk space is spanned by nodal basis functions defined by

$$\chi_j \in \mathbb{V}_{h,Y}, \quad \chi_j(X_k) = \delta_{jk} \quad \text{for } j, k = 1, \dots, J,$$

where δ_{jk} is the Kronecker delta and J is the number of nodes (vertices) $X_j \in Y$ of the tetrahedrons S_h . Then function $\Phi(t) \in \mathbb{V}_{h,Y}$ has the form

$$\Phi(t, x) = \sum_{j=1}^J a_j(t) \chi_j(x) \quad \text{for } x \in Y_h, \quad t \in (0, T),$$

with real measurable functions a_j . Similarly the surface finite element space is spanned by nodal basis functions

$$\mu_j \in \mathbb{V}_{h,\Gamma}, \quad \mu_j(Z_k) = \delta_{jk} \quad \text{for } j, k = 1, \dots, M,$$

where $Z_j \in \Gamma$, with $j, k = 1, \dots, M$, are nodes of the triangulated surface such that $Z_k = X_k \cap \Gamma_h \neq 0$. Then function $P(t) \in \mathbb{V}_{h,\Gamma}$ has the form

$$P(t, x) = \sum_{j=1}^M b_j(t) \mu_j(x) \quad \text{for } x \in \Gamma_h, t \in (0, T),$$

with real measurable functions b_j . Thus, the semi-discretized problem corresponding to (3)-(6) reads

$$\begin{aligned} \langle \partial_t \Phi_d, \Psi \rangle_{Y_h} + \langle D_1 \nabla \Phi_d, \nabla \Psi \rangle_{Y_h} + \langle C_1 \operatorname{tr}(\sigma(U))_+ \Phi_d, \Psi \rangle_{Y_h} + \langle n_r \tilde{k}_3 \Phi_d, \Psi \rangle_{\Gamma_h} &= \langle k_1 \Phi_a, \Psi \rangle_{Y_h}, \\ \langle \partial_t \Phi_a, \Psi \rangle_{Y_h} + \langle D_2 \nabla \Phi_a, \nabla \Psi \rangle_{Y_h} + \langle k_1 \Phi_a, \Psi \rangle_{Y_h} &= \langle C_1 \operatorname{tr}(\sigma(U))_+ \Phi_d, \Psi \rangle_{Y_h} + \langle n_r \tilde{k}_3 \Phi_d, \Psi \rangle_{\Gamma_h}, \\ \langle \partial_t P_a, W \rangle_{\Gamma_h} + \langle D_3 \nabla_{\Gamma_h} P_a, \nabla_{\Gamma_h} W \rangle_{\Gamma_h} + \langle \tilde{k}_4(\Phi_a) P_a, W \rangle_{\Gamma_h} &= \langle n_r \tilde{k}_5(\Phi_a), W \rangle_{\Gamma_h}, \\ \langle E(\Phi_a) \epsilon(U), \epsilon(V) \rangle_{Y_h} &= \langle k_6 \mathbb{P}(P_a \hat{\nu}), V \rangle_{\Gamma_h}, \end{aligned} \quad (\text{A3})$$

for every test function $\Psi \in \mathbb{V}_{h,Y}$, $W \in \mathbb{V}_{h,\Gamma}$ and $V \in \mathbb{W}_{h,Y}$.

To obtain the fully discrete problem we discretize (A3) in time using the backwards Euler method with

$$\partial_t \Phi \approx \frac{\Phi^n - \Phi^{n-1}}{\Delta t},$$

where $\Delta t = T/N$, and an IMEX time-stepping method, in which the diffusion terms are treated implicitly and the nonlinear reaction terms are treated explicitly [60]. The discrete system, with the notation $\Phi^n(x) = \Phi(t_n, x)$, reads

$$\begin{aligned} \langle \mathbb{E}(\Phi_a^{n-1}) \epsilon(U^n), \epsilon(V) \rangle_{Y_h} &= \langle k_6 \mathbb{P}(P_a^{n-1} \hat{\nu}), V \rangle_{\Gamma_h}, \\ \Delta t^{-1} \langle \Phi_d^n, \Psi \rangle_{Y_h} + \langle D_1 \nabla \Phi_d^n, \nabla \Psi \rangle_{Y_h} &+ \langle C_1 \operatorname{tr}(\sigma(U^n))_+ \Phi_d^n, \Psi \rangle_{Y_h} + \langle n_r \tilde{k}_3 \Phi_d^n, \Psi \rangle_{\Gamma_h} \\ &= \Delta t^{-1} \langle \Phi_d^{n-1}, \Psi \rangle_{Y_h} + \langle k_1 \Phi_a^{n-1}, \Psi \rangle_{Y_h}, \\ \Delta t^{-1} \langle \Phi_a^n, \Psi \rangle_{Y_h} + \langle D_2 \nabla \Phi_a^n, \nabla \Psi \rangle_{Y_h} &+ \langle k_1 \Phi_a^n, \Psi \rangle_{Y_h} \\ &= \Delta t^{-1} \langle \Phi_a^{n-1}, \Psi \rangle_{Y_h} + \langle C_1 \operatorname{tr}(\sigma(U^n))_+ \Phi_d^n, \Psi \rangle_{Y_h} + \langle n_r \tilde{k}_3 \Phi_d^n, \Psi \rangle_{\Gamma_h}, \\ \Delta t^{-1} \langle P_a^n, W \rangle_{\Gamma_h} + \langle D_3 \nabla_{\Gamma_h} P_a^n, \nabla_{\Gamma_h} W \rangle_{\Gamma_h} &+ \langle \tilde{k}_4(\Phi_a^n) P_a^n, W \rangle_{\Gamma_h} \\ &= \Delta t^{-1} \langle P_a^{n-1}, W \rangle_{\Gamma_h} + \langle n_r \tilde{k}_5(\Phi_a^n), W \rangle_{\Gamma_h}. \end{aligned} \quad (\text{A4})$$

To benchmark the numerical scheme and implementation in FEniCS, we consider Y to be a unit ball and a simplified model

$$\begin{aligned} -\nabla \cdot \sigma(u) &= f && \text{in } Y, \\ \sigma(u) \cdot \nu &= \mathbb{P}(g\rho) && \text{on } \Gamma, \\ \partial_t \phi - \Delta \phi &= q_1 + \operatorname{tr}(\sigma(u))_+ && \text{in } Y, t > 0, \\ \nabla \phi \cdot \nu &= \rho - \phi && \text{on } \Gamma, t > 0, \\ \partial_t \rho - \Delta \rho &= q_2 - \rho + \phi && \text{on } \Gamma, t > 0, \\ u(0, x) &= u_{ex}(0, x), \quad \phi(0, x) = \phi_{ex}(0, x) && \text{in } Y, \\ \rho(0, x) &= \rho_{ex}(0, x) && \text{on } \Gamma. \end{aligned} \quad (\text{A5})$$

The functions f , g , q_1 , and q_2 are such that

$$\begin{aligned} u_{ex}(t, x) &= (2x_1^2 x_2 x_3 e^{-4t}, -x_1 x_2^2 x_3 e^{-4t}, -2x_1 x_2 x_3^2 e^{-4t}), \\ \phi_{ex}(t, x) &= \cos(x_1 x_2 x_3) e^{-4t}, \\ \rho_{ex}(t, x) &= \cos(x_1 x_2 x_3) e^{-4t} - 3 \sin(x_1 x_2 x_3) e^{-4t} \end{aligned}$$

is the exact solution of (A5). Then for the experimental order of convergence

$$\text{EOC} = \frac{\log(e_n/e_{n-1})}{\log(h_n/h_{n-1})},$$

where h_n , for $n = 1, 2, 3, 4$, are given in Table (A2) and e_n is the error in the L^2 -norm or the H^1 -norm, we obtain the second order of convergence in the L^2 -norm and first order of convergence in H^1 -norm, see Table A3.

0.64009064	0.51659533	0.26133991	0.13143219	
------------	------------	------------	------------	--

Table A2: Four mesh sizes used in the calculation of EOC.

EOC for L^2 norm for ϕ	1.63892969	1.77954013	1.93991995
EOC for H^1 norm for ϕ	1.44823967	1.68924575	1.89210920
EOC for L^2 norm for ρ	1.58078852	1.78119701	1.96179159
EOC for H^1 norm for ρ	1.78659381	1.49338646	1.52956398
EOC for L^2 norm for u	0.92059071	1.74758321	1.87989078
EOC for H^1 norm for u	1.05358979	1.40005535	1.27787725

Table A3: Experimental order of convergence for numerical scheme (A4) considered for model (A5).

A.4 Conversion from $\mu\text{mol}/\text{dm}^2$ to $\#/ \mu\text{m}^2$

Scott et al. [18] uses $\mu\text{mol}/\text{dm}^3$ for concentrations in the cytoplasm and $\#/ \mu\text{m}^2$ for concentrations on the plasma membrane, specifically for ρ_a . In the models derived and analysed in this work, we use $\mu\text{mol}/\text{dm}^3$ for concentrations in the cytoplasm and $\mu\text{mol}/\text{dm}^2$ for ρ_a . To be able to use the same initial conditions and to compare the results, we need to find a conversion from $\#/ \mu\text{m}^2$ to $\mu\text{mol}/\text{dm}^2$. We use the fact that the maximum value for ρ_a for large E is $11 \cdot 10^{-16} \mu\text{mol}/\mu\text{m}^2$ as given in [18, Fig 2B]. The maximum value in the numerical results for ρ_a for large E is $593 \#/ \mu\text{m}^2$ as given in [18, Fig 3C(ii)] and assume these are equivalent. This relation gives the conversion

$$10^{-5} \frac{\mu\text{mol}}{\text{dm}^2} = 10^{-15} \frac{\mu\text{mol}}{\mu\text{m}^2} = \frac{5930}{11} \#/ \mu\text{m}^2 = 539.09 \#/ \mu\text{m}^2. \quad (\text{A6})$$

A.5 Simulations with nucleus

To model the inclusion of a nucleus in the cell, we consider the model equations (3) and (6) in $Y \setminus \bar{Y}_{\text{nc}}$, where domain Y_{nc} represents the nucleus. We choose zero flux boundary conditions for ϕ_d and ϕ_a on ∂Y_{nc} . For the mechanics, we choose the interior boundary condition to model the fact that the nucleus is hard to deform

$$\sigma(u)\nu = -\omega u \quad \text{on } \partial Y_{\text{nc}}, \quad (\text{A7})$$

where ω is a positive constant determining the rigidity of the nucleus.

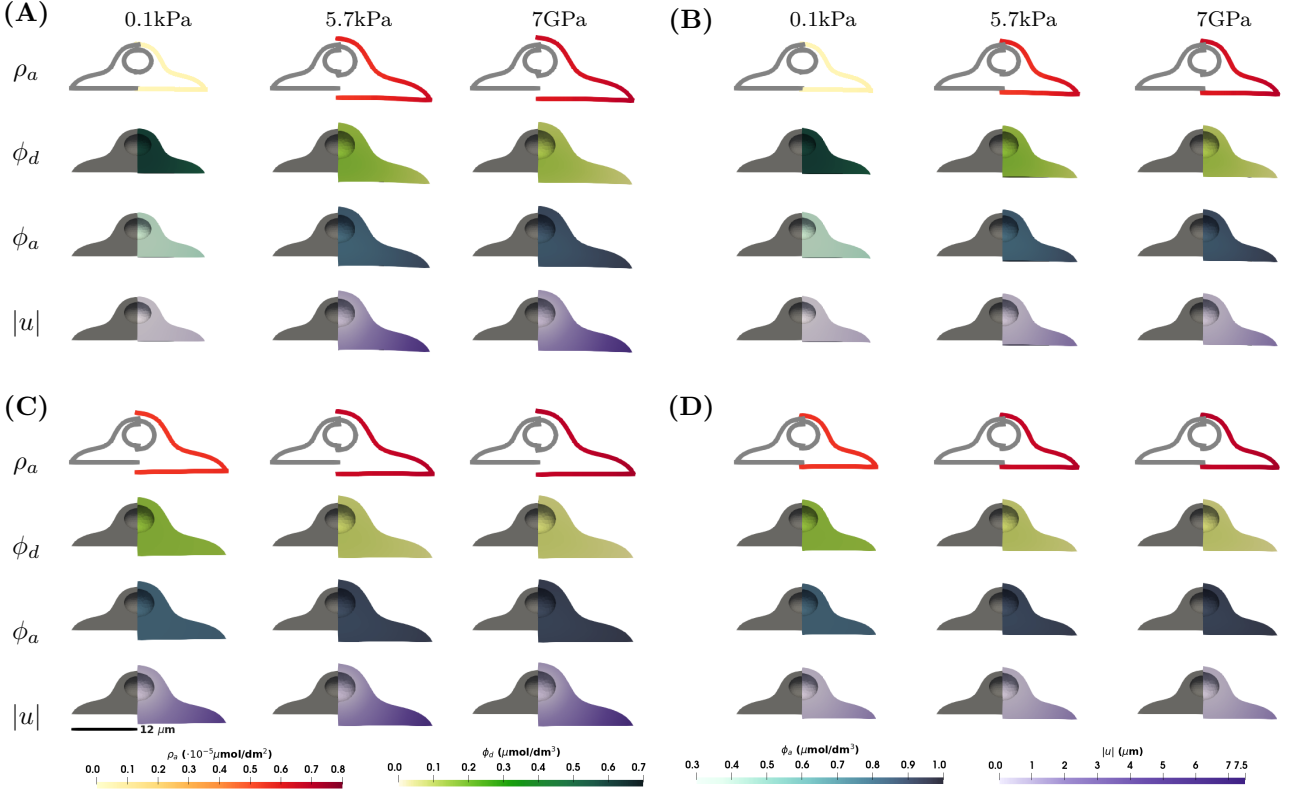


Figure A7: Numerical simulation results showing ρ_a , ϕ_d , ϕ_a and $|u|$ for model (3), (4), (6), and (A7) for the axisymmetric shape with a nucleus and in the case of the 3D stimulus at a steady state at $T = 100$ s. Four different scenarios are considered: (A) $C_1 = 0$ (kPa s) $^{-1}$ ($\sigma \not\rightarrow \phi_a$) and $E_c = 0.6$ kPa ($\phi_a \not\rightarrow E_c$); (B) $C_1 = 0$ (kPa s) $^{-1}$ ($\sigma \not\rightarrow \phi_a$) and $E_c = f(\phi_a)$ ($\phi_a \rightarrow E_c$); (C) $C_1 = 0.1$ (kPa s) $^{-1}$ ($\sigma \rightarrow \phi_a$) and $E_c = 0.6$ kPa ($\phi_a \not\rightarrow E_c$); (D) $C_1 = 0.1$ (kPa s) $^{-1}$ ($\sigma \rightarrow \phi_a$) and $E_c = f(\phi_a)$ ($\phi_a \rightarrow E_c$). Within each subfigure, the rows represent ρ_a , ϕ_d , ϕ_a and $|u|$ on a cross-section of the plane $x_1 = 0$ of the axisymmetric cell, and the columns represent $E = 0.1, 5.7, 7 \cdot 10^6$ kPa. Parameter values as in Table 1, and $\omega = 1$. The corresponding results without a nucleus can be found in Fig 6.

A.6 Parameter sensitivity analysis

As we compare and extend upon the model of [18], we have used the same parameter values where possible. For all new values introduced in this work, see Table 1, we provide here a simple parameter sensitivity analysis to explore how different choices of these parameters would affect the results. We choose to focus on the case of the 3D stimulus for the model in Eqs (3)-(4), (6) with force boundary conditions on the whole cell membrane for the axisymmetric cell, where $E_c = f(\phi_a)$ and $C_1 = 0.1$ (kPa s) $^{-1}$ when not otherwise specified, and for $E = 0.1$ kPa, 5.7 kPa, 7 GPa. Parameter values are chosen as in Table 1 and we show summary statistics for a 10% and 20% change in values for each of the following parameters separately: C_1 , k_6 , k_7 , k_8 , p and ν_c .

In Fig A8, we see all parameters only have a small effect on the concentrations of ϕ_a and ρ_a with C_1 and k_6 being the most influential when $E = 0.1$ kPa. The parameters k_7 , k_8 , p and ν_c are part of the equations of linear elasticity and therefore their effect would be through changes in the stress in the reaction term of ϕ_a , which is also determined by C_1 . The change in the stress due to the change in these parameters barely changes the results of the signalling molecules. Next to that, we see that the effect is larger for smaller substrate stiffness E , which could be due to the fact that ϕ_a and ρ_a are already close to their maximum values for larger substrate stiffnesses. Fig A8 shows that the effect of C_1 on the change in ρ_a is approximately tripled compared to the change in ϕ_a . This could be because the reaction term including ϕ_a in ρ_a is to the power of 5.

Fig A8 also shows that k_7 , k_8 , and p have an opposite effect on the cell stiffness E_c and the change in volume $\text{div}(u)$, where an increase in these parameters increases the stiffness and decreases $\text{div}(u)$. The parameter k_8 has the largest effect on these variables, where a -20% change has a tripling effect of a +60% change in $\text{div}(u)$. Lastly, we see that ν_c only significantly changes $\text{div}(u)$. The effect that ν_c , the Poisson ratio, determining the ratio between the transverse and the axial strain, has on the volume change does not seem to induce changes in other variables.

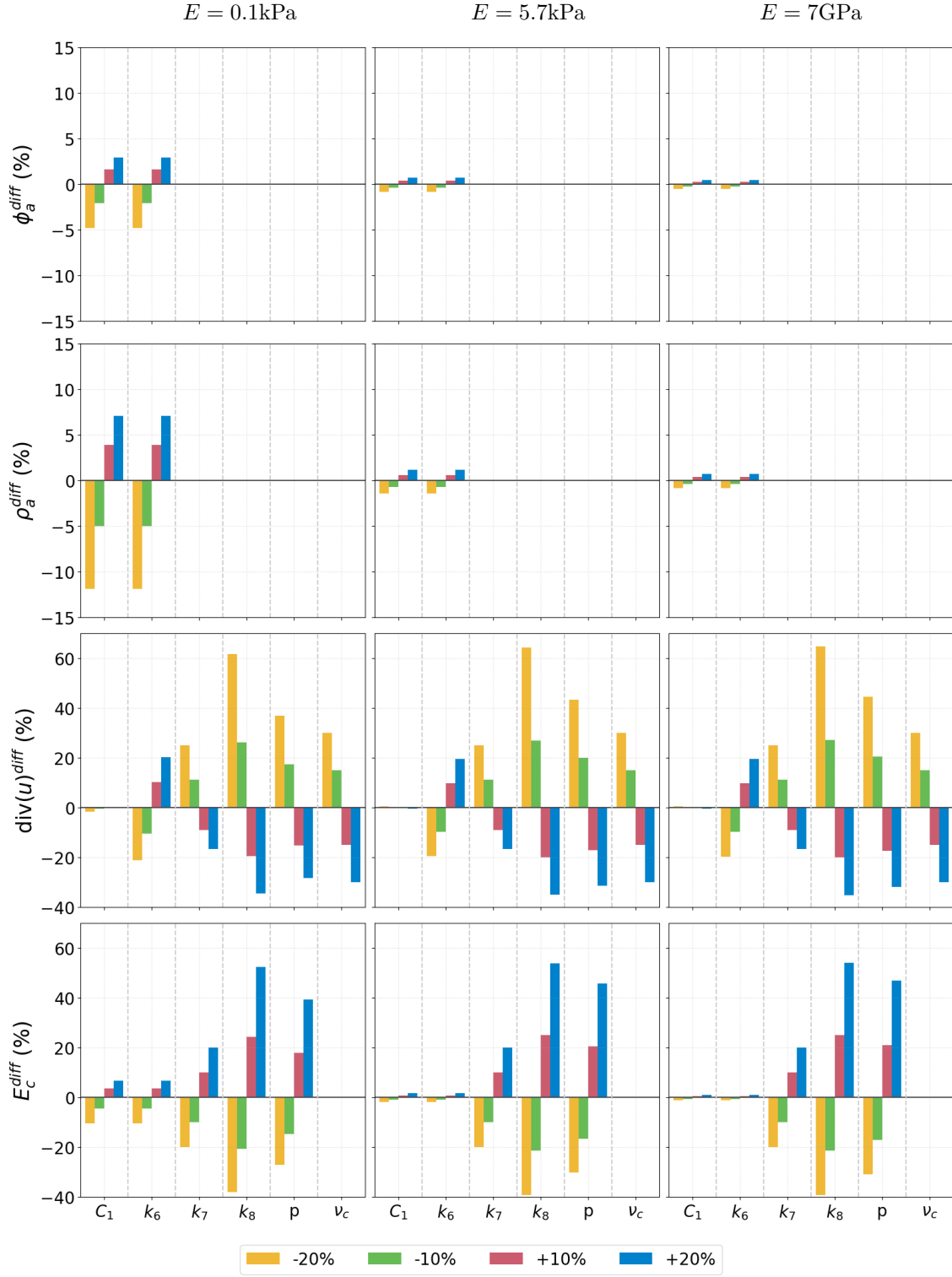


Figure A8: **Parameter sensitivity analysis results showing the percentage change in the means of $f(\phi_a)$, $\text{div}(u)$, ϕ_a and ρ_a (%) as response to a percentage change in the parameters C_1 , k_6 , k_7 , k_8 , p and ν_c .** Here, the percentage change in the mean is defined as $v^{\text{diff}} = \frac{\int_{\Omega} v \text{d}x - \int_{\Omega} v^* \text{d}x}{\int_{\Omega} v^* \text{d}x} \cdot 100$, where v the new result and v^* the original result for parameters in Table 1. These results are for the model (3), (4), and (6), for the axisymmetric shape and in the case of the 3D stimulus at $T = 100$ s by which time the results are at a steady state. The columns represent different values for the substrate stiffness E and the rows represent the percentage change in the mean of the variables ϕ_a , ρ_a , $\text{div}(u)$ and $E_c = f(\phi_a)$. If not otherwise specified, parameter values are as in Table 1. The corresponding simulation results can be found in Fig 6.

A.7 Simulations with linear viscoelasticity

To model a linear viscoelastic material, we consider the model equations (3) and (6) with the stress defined as

$$\sigma(u) = \lambda(\phi_a)(\nabla \cdot u + \theta_\lambda \nabla \cdot \partial_t u)I + 2\mu(\phi_a) ((\nabla u + (\nabla u)^T) + \theta_\mu(\nabla \partial_t u + (\nabla \partial_t u)^T)), \quad (\text{A8})$$

with the initial condition $u(0, x) = 0$ for $x \in Y$, where θ_λ and θ_μ are the characteristic retardation times. We use a backward Euler discretization such that

$$\begin{aligned} & \langle \lambda(\Phi_a^{n-1})(1 + \Delta t^{-1}\theta_\lambda)(\nabla \cdot U^n)I + 2\mu(\Phi_a^{n-1})(1 + \Delta t^{-1}\theta_\mu)\epsilon(U^n), \epsilon(V) \rangle_{Y_h} \\ &= \Delta t^{-1} \langle \lambda(\Phi_a^{n-1})\theta_\lambda(\nabla \cdot U^{n-1})I + 2\mu(\Phi_a^{n-1})\theta_\mu\epsilon(U^{n-1}), \epsilon(V) \rangle_{Y_h} + \langle k_6 \mathbb{P}(P_a^{n-1}\hat{\nu}), V \rangle_{\Gamma_h}. \end{aligned}$$

The numerical simulation results are presented in Fig A9.

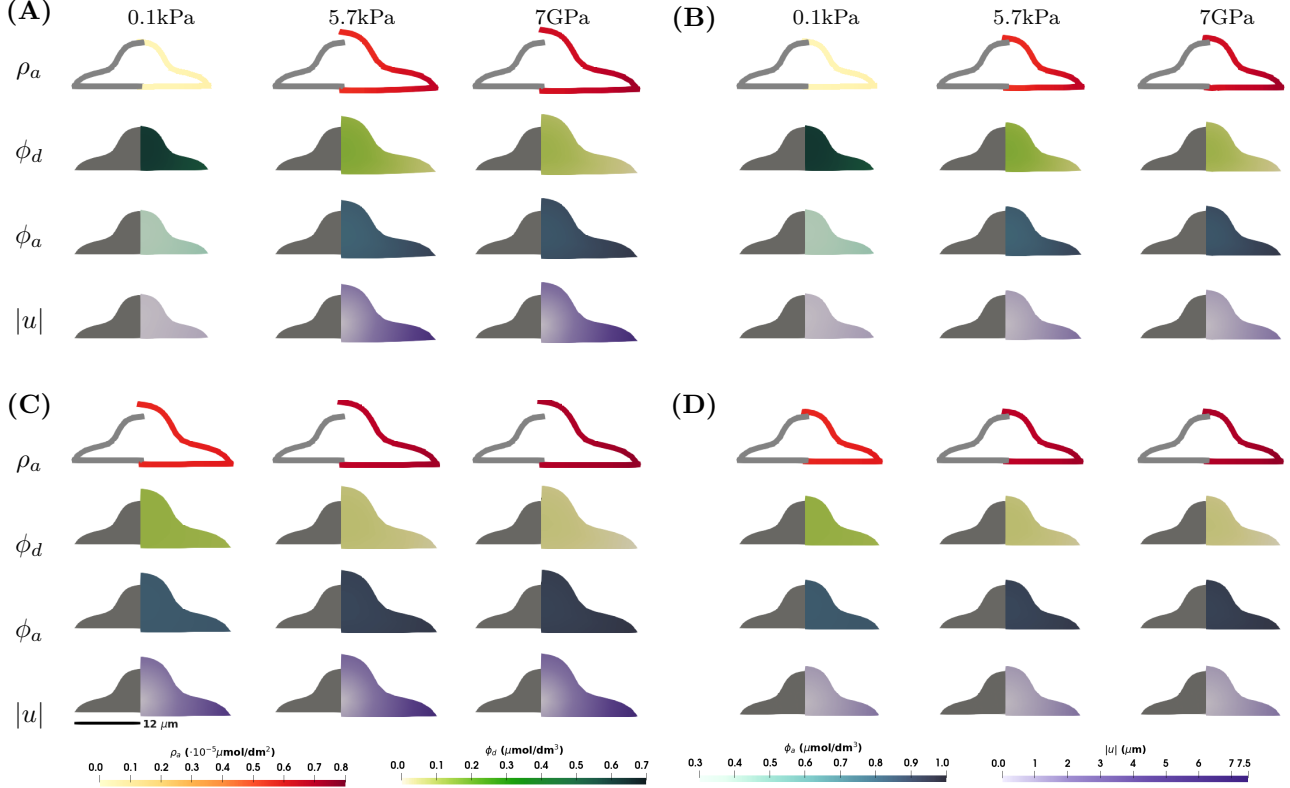


Figure A9: Numerical simulation results showing ρ_a , ϕ_d , ϕ_a and $|u|$ for model (3), (4), (6), and (A8) for the axisymmetric shape and in the case of the 3D stimulus at a steady state at $T = 100$ s. Four different scenarios are considered: (A) $C_1 = 0$ $(\text{kPa s})^{-1}$ ($\sigma \not\rightarrow \phi_a$) and $E_c = 0.6$ kPa ($\phi_a \not\rightarrow E_c$); (B) $C_1 = 0$ $(\text{kPa s})^{-1}$ ($\sigma \not\rightarrow \phi_a$) and $E_c = f(\phi_a)$ ($\phi_a \rightarrow E_c$); (C) $C_1 = 0.1$ $(\text{kPa s})^{-1}$ ($\sigma \rightarrow \phi_a$) and $E_c = 0.6$ kPa ($\phi_a \not\rightarrow E_c$); (D) $C_1 = 0.1$ $(\text{kPa s})^{-1}$ ($\sigma \rightarrow \phi_a$) and $E_c = f(\phi_a)$ ($\phi_a \rightarrow E_c$). Within each subfigure, the rows represent ρ_a , ϕ_d , ϕ_a and $|u|$ on a cross-section of the plane $x_1 = 0$ of the axisymmetric cell, and the columns represent $E = 0.1, 5.7, 7 \cdot 10^6$ kPa. Parameter values as in Table 1, and $\theta_\lambda = \theta_\mu = 1$. The corresponding results with only elastic stress can be found in Fig 6.